Applied Mathematical Modelling 114 (2023) 694–721

Contents lists available at ScienceDirect

Applied Mathematical Modelling

journal homepage: www.elsevier.com/locate/apm

The optimal design of dynamic systems with negative stiffness inertial amplifier tuned mass dampers

Sudip Chowdhury[a,1], Arnab Banerjee[a,2,*], Sondipon Adhikari[b,3]

[a] Civil Engineering Department, Indian Institute of Technology Delhi (IITD), India
[b] James Watt School of Engineering, The University of Glasgow, Glasgow, Scotland, UK

A R T I C L E   I N F O

Article history:
Received 6 October 2021
Revised 2 October 2022
Accepted 6 October 2022
Available online 15 October 2022

Keywords:
Nonlinear negative stiffness inertial amplifier tuned mass dampers
Nonlinear negative stiffness tuned mass dampers
Nonlinear inertial amplifier tuned mass dampers
Exact closed-form

A B S T R A C T

The negative stiffness inertial amplifier tuned mass dampers (NSIA-TMD) are introduced in this paper. Another two novel tuned mass dampers such as negative stiffness tuned mass damper (NS-TMD) and inertial amplifier tuned mass damper (IA-TMD) are mathematically developed from the negative stiffness inertial amplifier tuned mass dampers (NSIA-TMD) and the static masses of these three novel dampers are retained constant. The exact closed-form expressions for optimized system parameters for these novel dampers are obtained using H_2 and H_∞ optimization techniques. The dynamic responses of the SDOF systems controlled by H_2 and H_∞ optimized novel tuned mass dampers subjected to base excitations are obtained analytically. The dynamic response reduction capacities of the novel tuned mass dampers are compared with the dynamic response reduction capacities of traditional tuned mass dampers (TMD). Therefore, the dynamic response reduction capacities of H_2 optimized NS-TMD, NSIA-TMD, and IA-TMD are significantly 45.51%, 43.47%, 41.08% superior to the H_2 optimized traditional tuned mass dampers. Furthermore, the dynamic response reduction capacities of H_∞ optimized NS-TMD, NSIA-TMD, and IA-TMD are significantly 3.31%, 8.98%, 13.79% superior to the H_∞ optimized traditional tuned mass dampers. The nonlinear negative stiffness inertial amplifier tuned mass dampers (NNSIA-TMD) are also introduced in this paper. As a result, the dynamic response reduction capacities of H_2 optimized nonlinear negative stiffness tuned mass damper (NNS-TMD), NNSIA-TMD, and nonlinear inertial amplifier tuned mass damper (NIA-TMD) are significantly 24.54%, 21.92%, 19.12% superior to the H_2 optimized traditional tuned mass dampers. Furthermore, the dynamic response reduction capacities of H_∞ optimized NNS-TMD, NNSIA-TMD, and NIA-TMD are significantly 3.01%, 9.04%, 15.08% superior to the H_∞ optimized traditional tuned mass dampers. The outcomes of this research are mathematically accurate and relevant to practical design applications.

* Corresponding author.
E-mail address: abanerjee@iitd.ac.in (A. Banerjee).
[1] https://orcid.org/0000-0001-6218-4843
[2] https://orcid.org/0000-0002-3157-6200
[3] http://orcid.org/0000-0003-4181-3457

https://doi.org/10.1016/j.apm.2022.10.011
0307-904X/

1. Introduction

The passive vibration control devices have been introduced to protect the structures and human lives from natural calamities like seismic events or cyclones. Tuned mass dampers (TMD) are one of these devices which provide significant resistance against vibration. Frahm [1] first patented the theory of TMD in 1909 without considering damping in TMD. A undamped TMD is considerably effective when the natural frequency of TMD is near to the excitation frequency, but lack of vibration reduction occurs when excitation frequency deviates away from the natural frequency of TMD. Ormondroyd and Den Hartog later incorporated damped TMD and established closed-form formulas for optimal design parameters [2]. The H_∞ optimization method is based on fixed-point theory. This method is appropriate for harmonically excited structures [3–6]. Den Hartog's book illustrates this strategy thoroughly [7]. Since then, TMD has been extensively researched and utilized in mechanical and civil applications such as automotive suspension systems, offshore platforms, buildings, and bridges [8–15]. H_2 optimization is employed to determine optimal design parameters [16] when the controlled structure is subjected to white-noise random excitation [17–27]. Previous study shows a TMD's capacity to suppress vibrations improves with mass.

Smith has introduced a mechanical mechanism called an inerter to reduce structural vibrations [28,29]. This inerter has been induced into or in parallel with conventional passive vibration control devices to enhance its energy dissipation capacity by amplifying the substantial effective mass through rotating mass [30–33]. Inerters are used to increase the performance of mechanical engineering machinery and parts, notably automotive and train suspensions [34–36]. Inspired by the successful application in the mechanical engineering field, inerter have also applied in civil engineering structures, and many researchers have achieved positive outcomes [37,38]. In particular, inerters have been implanted in the classical tuned mass damper [39–47] and base isolator to control the vibration response of different dynamic systems [48–54]. In this paper, the main focus will be on TMDs. In fact, the most of the research on inerter-based tuned mass dampers is conducted based on using a flywheel-gear inerter [39,47]. Furthermore, inertial amplifiers are mass amplification devices [55,56] that can increase effective system properties such as effective mass, stiffness, and damping of vibration control devices to increase their dynamic response reduction capacity [57–60]. Apart from the effective mass amplification devices, the dynamic response reduction capacity of conventional vibration control devices is amplified using negative stiffness and negative mass devices [61–75]. The combination of mass amplification and negative stiffness devices is observed in the metamaterial field [76–84]. For mitigating the dynamic responses of the structures, the mass amplification and negative stiffness devices are individually applied to the passive vibration control devices [85–93]. Overall state of the art shows that the combination of inertial amplifiers and negative stiffness devices have not been applied to any conventional tuned mass dampers for enhancing their dynamic response capacity. A research gap has been identified from the state of the art.

Therefore, the negative stiffness inertial amplifier tuned mass dampers (NSIA-TMD), negative stiffness tuned mass damper (NS-TMD), and inertial amplifier tuned mass damper (IA-TMD) are introduced in this paper, which are not presented in any previous research as per the author's best knowledge. These novel tuned mass dampers are equipped with single degree of freedom systems for accessing their exact dynamic response reduction capacity. H_2 and H_∞ optimization techniques are applied to evaluate the optimal system parameters for these novel tuned mass dampers analytically [94]. The nonlinear negative stiffness inertial amplifier tuned mass damper (NNSIA-TMD), nonlinear negative stiffness tuned mass damper (NNS-TMD), and nonlinear inertial amplifier tuned mass damper (NIA-TMD) for single degree of freedom systems (SDOF) are also introduced in this paper. The dynamic response reduction capacities of H_2 and H_∞ optimized novel tuned mass dampers are compared with the dynamic response reduction capacities of H_2 and H_∞ optimized traditional tuned mass dampers.

2. Methodology

2.1. Proposed novel tuned mass dampers

The schematic diagram of a single degree of freedom system equipped with negative stiffness inertial amplifier tuned mass dampers (NSIA-TMD) has been displayed in Fig. 1(a). The individual schematic diagram of a negative stiffness inertial amplifier tuned mass damper (NSIA-TMD) has also been displayed in Fig. 1(b). The free-body diagrams for top triangular part kinematics under consideration in undeformed and deformed states have been shown in Fig. 1(c).

The free-body diagrams of the structural members of NSIA-TMD and the generation of inertial forces have been shown in Fig. 1(d). The schematic diagrams of a single degree of freedom system equipped with negative stiffness tuned mass dampers (NS-TMD) and inertial amplifier tuned mass dampers (IA-TMD) have been displayed in Fig. 1(e) and (f).The dynamic effective mass for these novel tuned mass dampers has been derived using these free-body diagrams. Another structural parameter has been introduced in this paper, namely the mass tuning ratio of NSIA-TMD, which denotes μ. The other two novel tuned mass dampers, namely negative stiffness tuned mass damper (NS-TMD) and inertial amplifier tuned mass damper (IA-TMD) are mathematically formulated by altering the mass tuning ratio. The static mass, stiffness, and damping of these novel negative stiffness tuned mass dampers are denoted by the variables m_d, k_d, and c_d. The effective mass, effective stiffness, and effective damping of these novel negative stiffness tuned mass dampers are denoted by the variables m_{ad}, k_{ad}, and c_{ad}. m_a, m_b, and k_b refer to the static masses and stiffness of the mass-spring-mass system. The negative stiffness of the entire novel dampers has been generated through the vertical spring mass system attached to the amplifier's mass. $\ddot{x}_g$ denote for ground motion. All three novel dampers are installed at the top of a single degree of freedom system. m_s, k_s, and c_s refer to the mass, stiffness, and damping of the single degree of freedom system, which refers as "primary structure".

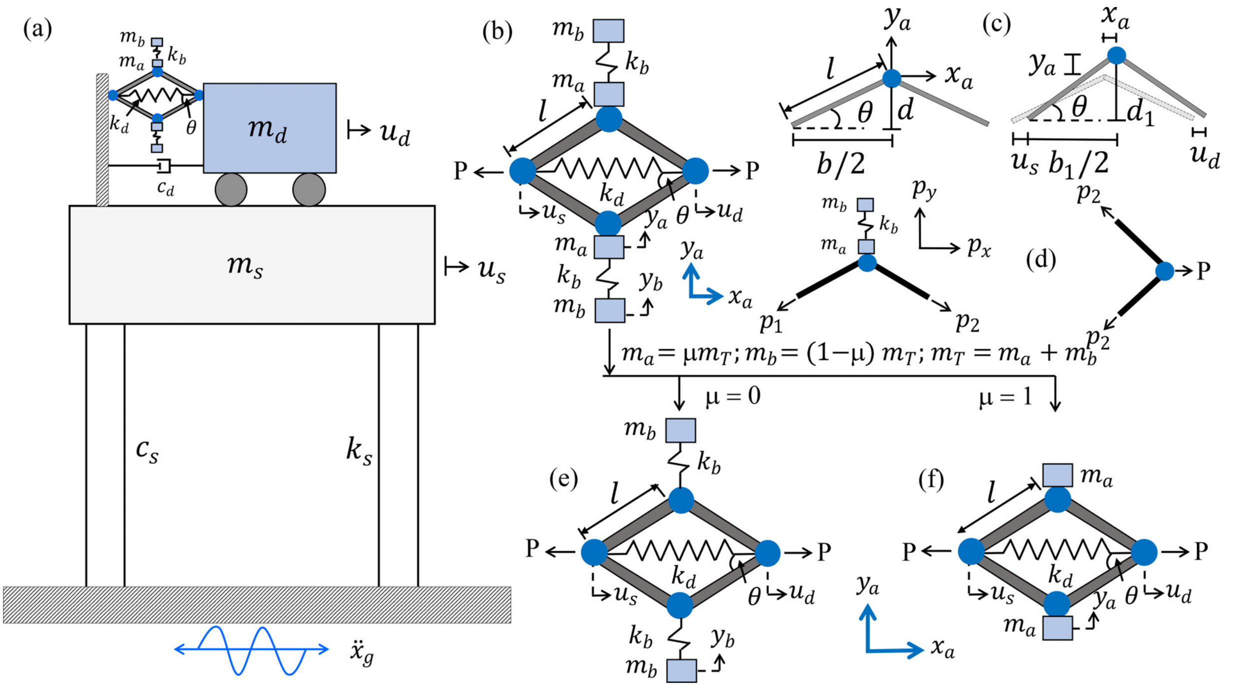

Fig. 1. (a) The schematic diagram of a single degree of freedom system equipped with negative stiffness inertial amplifier tuned mass dampers (NSIA-TMD), (b) Negative stiffness inertial amplifier tuned mass dampers (NSIA-TMD), (c) The free-body diagrams for top triangular part kinematics under undeformed and deformed states consideration. (d) The free-body diagrams of the structural members of NSIA-TMD and the generation of inertial forces. (e) The schematic diagram of negative stiffness tuned mass damper. (f) The schematic diagram of inertial amplifier tuned mass damper.

Table 1
The values for mass tuning ratio.

Mass tuning ratio	NS-TMD	NSIA-TMD	IA-TMD
μ	0	$0.1 \le \mu \le 0.9$	1.0

2.2. Equations of motion of novel tuned mass dampers

Total static mass of the controlled system vertical mass-spring-mass system derives as $m_T = m_a + m_b$. m_a and m_b are individually derived as

$$m_a = \mu m_T \quad \text{and} \quad m_b = (1-\mu)m_T \tag{1}$$

Applying μ, these novel tuned mass dampers have been mathematically formulated and the details values are listed in Table 1.

The mass tuning ratios for NS-TMD, NSIA-TMD, and NS-TMD are derived as $\mu = 0$, $0.1 \le \mu \le 0.9$, and $\mu = 1.0$. The equation of motion of the vertical spring-mass system attached to the amplifier's mass has been derived as

$$m_b\ddot{y}_b + k_b(y_b - y_a) = 0 \tag{2}$$

A small-amplitude vibration has been applied and the entire controlled structure moves towards the x-direction. As a result the small deflections for masses m_a and m_b are occur in x and y-directions. For y-direction, the steady stead solutions are considered as $y_a = Y_a e^{i\omega t}$, $y_b = Y_b e^{i\omega t}$ and substituted in Eq. (2). Hence, the dynamic response of spring-mass system derives as

$$Y_b = \left(\frac{k_b}{k_b - m_b\omega^2}\right)Y_a \tag{3}$$

It has been considered that the entire structure is in an equilibrium state and momentum balance has occurred in the y direction. As a result, the effective mass for the spring mass system derives

$$\begin{aligned} & m_e\dot{y}_a = m_b\dot{y}_b + m_a\dot{y}_a \\ \text{and} \quad & m_e = (1-\mu)m_T\left(\tfrac{k_b}{k_b - m_b\omega^2}\right) + \mu m_T = (1-\mu)m_T\left(\frac{1}{1-\frac{\omega^2}{\omega_b^2}}\right) + \mu m_T \end{aligned} \tag{4}$$

where m_e refers to the effective mass for the amplifier's mass, $\omega_b = \sqrt{k_b/m_b}$ refers to the natural frequency of the vertical spring-mass system attached to the amplifier's mass. The deformed mechanism of the negative stiffness inertial amplifier requires illustration for understanding the generation of dynamic negative effective properties such as mass and stiffness by the novel tuned mass dampers.

To perform that, the schematic diagram for the top triangular part of the novel tuned mass dampers have also been displayed in Fig. 1(c). Hence, the total displacement responses x_a and y_a for top triangular part of the novel tuned mass damper where the mass-spring-mass system installs, have been obtained using u_s, u_d, and θ. Using the effect of geometrical considerations, the displacement response x_a in horizontal direction has been derived as $x_a = (u_s + u_d)/2$. The displacement response in vertical direction y_a has been derived using the difference between the height of the top triangular part under undeformed and deformed states (i.e., $y_a = d_1 - d$). The values for d_1 and d have been determined using Pythagoras' theorem. Therefore, the detailed derivation has been illustrated below.

$$\begin{aligned} d_1^2 - d^2 &= \left(l^2 - \left(\frac{b_1}{2}\right)^2\right) - \left(l^2 - \left(\frac{b}{2}\right)^2\right) \\ &= \frac{1}{4}\left(2b(u_d - u_s) - (u_d - u_s)^2\right) \end{aligned} \tag{5}$$

Now the difference between vertical heights in squared terms for top triangular part at undeformed and deformed conditions has been written as $d_1^2 - d^2 = (d_1 + d)(d_1 - d) = (2d + y_a)y_a$. This expression has been substituted in Eq. (5) which leads to

$$(2d + y_a)y_a = \tfrac{1}{4}\left(2b(u_d - u_s) - (u_d - u_s)^2\right) \tag{6}$$

The left-hand side of Eq. (6) indicates that it's a quadratic equation. Eq. (6) also provides nonlinearity to the equations of motion for novel tuned mass dampers if large-amplitude vibration considers initially. The complexity will be arrived at while determining the optimized system parameters of novel tuned mass dampers analytically using H_2 and H_∞ optimization techniques. These analytical optimized system parameters of novel tuned mass dampers are significantly required for these kinds of novel passive vibration devices to achieve their robust dynamic response reduction capacity. These novel tuned mass dampers and their corresponding solutions are not presented in any state of the art. Therefore, to achieve the exact closed-form expressions for optimal design parameters of novel tuned mass dampers analytically using H_2 and H_∞ optimization methods, small-amplitude vibrations have been considered initially while forming equations of motion for these novel systems. Therefore, in the process of small-amplitude vibrations, these system have produced small deflections which enables to apply the linearized kinematics mechanism for these systems, respectively. Hence, the equations have been formed explicitly by considering $(u_d - u_s)^2 \ll 2b(u_d - u_s)$ and $y_a \ll b\tan\theta = d$. Therefore, the total displacement responses x_a and y_a for top and bottom triangular part of the novel tuned mass dampers have been derived as

$$x_a = \tfrac{u_s + u_d}{2} \quad \text{and} \quad y_a = \pm\tfrac{u_d - u_s}{2\tan\theta} \tag{7}$$

where x_a and y_a refer to the deflection of amplifier's effective mass m_e in x and y-directions. The inertial forces p_x and p_y generated by the effective mass m_e in x and y-directions at the top and bottom triangular parts of the novel tuned mass dampers have been derived as

$$p_x = m_e\ddot{x}_a \quad \text{and} \quad p_y = m_e\ddot{y}_a \tag{8}$$

The inertial forces develop through the rigid links p_1 and p_2 have been derived as

$$p_1 = \frac{1}{2}\left(\frac{p_y}{\sin\theta} - \frac{p_x}{\cos\theta}\right) \quad \text{and} \quad p_2 = \frac{1}{2}\left(\frac{p_y}{\sin\theta} + \frac{p_x}{\cos\theta}\right) \tag{9}$$

Using Eq. (9), the total reaction forces which have developed at the horizontal terminals through the rigid have been derived as

$$\begin{aligned} F &= 2p_2\cos\theta + k_d(u_d - u_s) \\ &= \underbrace{\frac{0.5m_e}{\tan^2\theta}}_{c_1}(\ddot{u}_d - \ddot{u}_s) + \underbrace{0.5m_e}_{c_2}(\ddot{u}_d + \ddot{u}_s) + k_{ad}(u_d - u_s) \end{aligned} \tag{10}$$

where $c_1 = \left(0.5m_e/\tan^2\theta\right)$ and $c_2 = 0.5m_e$ are the additional effective masses which have been have been added to the static mass of the novel tuned mass dampers m_d to produce the total dynamic effective masses of them [16]. Hence, the dynamic effective masses of the novel negative stiffness tuned mass damper derive as

$$\begin{aligned} m_{ad} &= m_d + 0.5m_e\left(1 + \frac{1}{\tan^2\theta}\right) \\ &= m_d + \Theta\left((1-\mu)m_T\left(\frac{\omega_b^2}{\omega_b^2 - \omega^2}\right) + \mu m_T\right) \end{aligned}$$

$$= \frac{m_1\,{\omega_b}^2 - m_2\,\omega^2}{{\omega_b}^2 - \omega^2} \tag{11}$$

where $m_1 = (\Theta\, m_T + m_d)$ and $m_2 = (\Theta\, m_T \mu + m_d)$, $\Theta = 0.5\left(1 + \frac{1}{\tan^2\theta}\right)$ are introduced for the simplified representation of Fig. 11. The dynamic effective stiffness of the novel tuned mass dampers derives as

$$k_{ad} = m_{ad}\omega_d^2 = \frac{m_1\,{\omega_b}^2\,\omega_d^2 - m_2\,\omega^2\,\omega_d^2}{{\omega_b}^2 - \omega^2} \tag{12}$$

where the dynamic negative stiffness generates through $(-m_2\,\omega^2\,\omega_d^2)$. Therefore, the generalized equations of motion for the single degree of freedom systems controlled by novel tuned mass dampers are determined as

$$\begin{aligned} m_{ad}\ddot{x}_d + c_{ad}\dot{x}_d + k_{ad}x_d + m_{ad}\ddot{x}_s &= -m_{ad}\ddot{x}_g \\ m_s\ddot{x}_s + c_s\dot{x}_s + k_s x_s - c_{ad}\dot{x}_d - k_{ad}x_d &= -m_s\ddot{x}_g \end{aligned} \tag{13}$$

$x_s = (u_s - x_g)$ and $x_d = (u_d - u_s)$ refer to the relative dynamic responses of the primary structure and novel tuned mass dampers. The steady state solutions for the dynamic responses of the primary structures and novel tuned mass dampers are considered as $x_s = X_s e^{\mathrm{i}\omega t}$, $x_d = X_d e^{\mathrm{i}\omega t}$, and $\ddot{x}_g = A_g e^{\mathrm{i}\omega t}$. $(\dot{\bullet})$ denotes the derivatives of variables w.r.t time. The steady state solutions are substituted in Eq. (13) and the transfer function has been derived as

$$\begin{bmatrix} \frac{(\mu_1\,{\omega_b}^2 + q^2\mu_2)(2\,q\zeta_d\,\omega_d + q^2 + {\omega_d}^2)}{q^2 + {\omega_b}^2} & \frac{q^2\,(\mu_1\,{\omega_b}^2 + q^2\mu_2)}{q^2 + {\omega_b}^2} \\ -\frac{(\mu_1\,{\omega_b}^2 + q^2\mu_2)\omega_d(2\,q\zeta_d + \omega_d)}{q^2 + {\omega_b}^2} & 2\,\zeta_s\,\omega_s\,q + q^2 + {\omega_s}^2 \end{bmatrix} \begin{Bmatrix} X_d \\ X_s \end{Bmatrix} = -\begin{bmatrix} \mu_{ad} \\ 1 \end{bmatrix} A_g \tag{14}$$

where $q = \mathrm{i}\omega$, $\mu_{ad} = (\mu_1\,{\omega_b}^2 + q^2\mu_2)/(q^2 + {\omega_b}^2)$, $\mu_1 = m_1/m_s = (\Theta\,\mu_T + \mu_d)$, $\mu_2 = m_2/m_s = (\Theta\,\mu_T\mu + \mu_d)$, and $\Theta = 0.5\left(1 + \frac{1}{\tan^2\theta}\right)$. μ_{ad} defines as the mass ratio of total effective mass m_{ad} to the SDOF system m_s, μ_T refers the mass ratio of the total static mass at lateral terminal to the SDOF system, μ_d denotes the ratio of static mass of NSIA-TMD to the SDOF system m_s. The dynamic response of the SDOF system is determined as

$$H_s(q) = \frac{X_s}{A_g} = \frac{\begin{array}{c} -q^4 + (-2\,\mu_2\,\zeta_d\,\omega_d - 2\,\zeta_d\,\omega_d)q^3 + \left(-{\omega_d}^2\mu_2 - {\omega_b}^2 - {\omega_d}^2\right)q^2 \\ +\left(-2\,\mu_1\,\zeta_d\,{\omega_b}^2\omega_d - 2\,\zeta_d\,{\omega_b}^2\omega_d\right)q - {\omega_b}^2{\omega_d}^2\mu_1 - {\omega_b}^2{\omega_d}^2 \end{array}}{\Delta_n} \tag{15}$$

Δ_n has been derived as

$$\Delta_n(q) = \begin{array}{c} q^6 + (2\,\mu_2\,\zeta_d\,\omega_d + 2\,\zeta_d\,\omega_d + 2\,\omega_s\,\zeta_s)q^5 + \left(4\,\zeta_d\,\zeta_s\,\omega_s\,\omega_d + \omega_d^2\mu_2 + \omega_b^2 + \omega_s^2 + \omega_d^2\right)q^4 \\ +\left(2\,\mu_1\,\zeta_d\,\omega_b^2\omega_d + 2\,\zeta_d\,\omega_b^2\omega_d + 2\,\zeta_d\,\omega_s^2\omega_d + 2\,\zeta_s\,\omega_b^2\omega_s + 2\,\omega_s\,\zeta_s\,\omega_d^2\right)q^3 \\ +\left(4\,\zeta_d\,\zeta_s\,\omega_b^2\omega_s\,\omega_d + \omega_b^2\omega_d^2\mu_1 + \omega_b^2\omega_s^2 + \omega_b^2\omega_d^2 + \omega_s^2\omega_d^2\right)q^2 \\ +\left(2\,\zeta_d\,\omega_b^2\omega_s^2\omega_d + 2\,\zeta_s\,\omega_b^2\omega_s\,\omega_d^2\right)q + \omega_b^2\omega_s^2\omega_d^2 \end{array} \tag{16}$$

The dynamic responses of the novel tuned mass dampers and the shear force of the entire controlled structures are listed in Appendix A.

2.3. Effective mass formulation for novel tuned mass dampers

The total static mass of the novel tuned mass dampers is derived as $m_d + 2m_T$. The advantages of the negative stiffness inertial amplifiers on the static property, such as mass and stiffness, have also been obtained mathematically. The ratio of the one side vertical total mass to the total static mass of the novel tuned mass dampers are derived as

$$\alpha = \frac{m_T}{m_d + 2m_T} \quad \text{and} \quad m_T = \left(\frac{\alpha}{1 - 2\alpha}\right)m_d \tag{17}$$

The ratio of the static mass to the total static mass of the novel tuned mass dampers are derived as

$$\beta = \frac{m_d}{m_d + 2m_T} = (1 - 2\alpha) \tag{18}$$

where m_d also represents as "damper mass". The dynamic effective mass ratio of the novel tuned mass dampers are derived as

$$\begin{aligned} \mu_f &= \frac{m_d}{m_d + 2m_T} + \frac{m_T}{m_d + 2m_T}\Theta\left((1 - \mu)\left(\frac{\omega_b^2}{\omega_b^2 - \omega^2}\right) + \mu\right) \\ &= (1 - 2\alpha) + \alpha\Theta\left((1 - \mu)\left(\frac{1}{1 - \frac{\eta^2}{\eta_b^2}}\right) + \mu\right) \end{aligned} \tag{19}$$

where μ_f refers to the total dynamic mass to the total static mass of the novel tuned mass damper. At initial condition, $\eta/\eta_b = 0$. Therefore, Eq. (19) has been modified as

$$\mu_{fs} = (1 - 2\alpha) + \alpha\Theta \tag{20}$$

where μ_{fs} refers to the static effective mass ratio. $\Theta = 0.5\left(1 + \frac{1}{\tan^2\theta}\right)$ and θ refers to the inertial angle. $\eta = \omega/\omega_s$ refers to the ratio of excitation frequency to the natural frequency of the primary structure. $\eta_b = \omega_b/\omega_s$ refers to the ratio of the vertical spring mass system to the primary structure.

2.4. Effective stiffness formulation for novel tuned mass dampers

The ratio of dynamic effective stiffness to the static effective stiffness of the novel tuned mass damper has been derived as

$$\kappa_f = \frac{k_{ad}}{k_d} = \frac{m_1\,{\omega_b}^2\,\omega_d^2 - m_2\,\omega^2\,\omega_d^2}{m_d\omega_d^2\left({\omega_b}^2 - \omega^2\right)} \tag{21}$$

k_{ad} and k_d of Eq. (21) are divided by $m_s\omega_s^4$. Therefore, κ_f has been non-dimensionalized as

$$\kappa_f = \frac{\eta_d^2{\eta_b}^2\mu_1 - \eta_d^2\eta^2\mu_2}{\left(\mu_d\eta_d^2\right)\left({\eta_b}^2 - \eta^2\right)} = \frac{\Theta\left(\frac{\mu_T}{\mu_d}\right) + 1 - \left(\frac{\eta^2}{\eta_b^2}\right)\Theta\left(\frac{\mu_T}{\mu_d}\right)\mu - \left(\frac{\eta^2}{\eta_b^2}\right)}{\left(1 - \left(\frac{\eta^2}{\eta_b^2}\right)\right)} \tag{22}$$

where $\mu_1 = (\Theta\,\mu_T + \mu_d)$, $\mu_2 = (\Theta\,\mu_T\mu + \mu_d)$, $\Theta = 0.5\left(1 + \frac{1}{\tan^2\theta}\right)$, and $\mu_T = m_T/m_s$ and the governing parameters are μ_d, μ, θ, and μ_T. At initial condition, $\eta/\eta_b = 0$. Therefore, Eq. (22) has been modified as

$$\kappa_{fs} = 0.5\left(1 + \frac{1}{\tan^2\theta}\right)\left(\frac{\mu_T}{\mu_d}\right) + 1 \tag{23}$$

where κ_{fs} refers to the static effective stiffness ratio.

2.5. H_2 optimization for novel tuned mass dampers

H_2 optimization technique has been applied to minimize the standard deviation of the dynamic responses of the primary structure [16,95]. The main dynamic system's damping has been considered zero to perform the H_2 optimization technique. Hence, after considering $\zeta_s = 0$ for Eq. (16), $\Delta_n(q)$ has been modified as

$$\Delta_n(q) = \begin{array}{c} q^6 + (2\,\mu_2\,\zeta_d\,\omega_d + 2\,\zeta_d\,\omega_d)q^5 + \left(\mu_2\,\omega_d^2 + \omega_b^2 + \omega_s^2 + \omega_d^2\right)q^4 \\ +\left(2\,\mu_1\,\zeta_d\,\omega_b^2\omega_d + 2\,\zeta_d\,\omega_b^2\omega_d + 2\,\zeta_d\,\omega_s^2\omega_d\right)q^3 + \left(\mu_1\,\omega_b^2\omega_d^2 + \omega_b^2\omega_s^2 + \omega_b^2\omega_d^2 + \omega_s^2\omega_d^2\right)q^2 \\ +2\,q\zeta_d\,\omega_b^2\omega_s^2\omega_d + \omega_b^2\omega_s^2\omega_d^2 \end{array} \tag{24}$$

where $q = \mathrm{i}\omega$. Hence, Eq. (24) is a 6th order polynomial equation and the standard deviation of the dynamic responses of the primary structures [16,95] have been derived as

$$\sigma_{x_s}^2 = \frac{S_0\pi\left(\begin{array}{c} 4\,\mu_1^3\zeta_d^2\omega_b^6\omega_s^2\omega_d^2 - 4\,\mu_1^2\mu_2\,\zeta_d^2\omega_b^4\omega_s^4\omega_d^2 + \mu_1^4\omega_b^6\omega_d^4 \\ +12\,\mu_1^2\zeta_d^2\omega_b^6\omega_s^2\omega_d^2 + 4\,\mu_1^2\zeta_d^2\omega_b^4\omega_s^4\omega_d^2 - 16\,\mu_1\,\mu_2\,\zeta_d^2\omega_b^4\omega_s^4\omega_d^2 \\ -4\,\mu_1\,\mu_2\,\zeta_d^2\omega_b^2\omega_s^6\omega_d^2 + 4\,\mu_2^2\zeta_d^2\omega_b^2\omega_s^6\omega_d^2 + \mu_1^3\omega_b^6\omega_s^2\omega_d^2 \\ +4\,\mu_1^3\omega_b^6\omega_d^4 + 2\,\mu_1^3\omega_b^4\omega_s^2\omega_d^4 - \mu_1^2\mu_2\,\omega_b^4\omega_s^4\omega_d^2 \\ -6\,\mu_1^2\mu_2\,\omega_b^4\omega_s^2\omega_d^4 - 2\,\mu_1^2\mu_2\,\omega_b^2\omega_s^4\omega_d^4 + 2\,\mu_1\,\mu_2^2\omega_b^2\omega_s^4\omega_d^4 \\ +12\,\mu_1\,\zeta_d^2\omega_b^6\omega_s^2\omega_d^2 - 12\,\mu_2\,\zeta_d^2\omega_b^4\omega_s^4\omega_d^2 + 6\,\mu_1^2\omega_b^6\omega_d^4 \\ +\mu_1^2\omega_b^2\omega_s^4\omega_d^4 - 9\,\mu_1\,\mu_2\,\omega_b^4\omega_s^2\omega_d^4 - 4\,\mu_1\,\mu_2\,\omega_b^2\omega_s^4\omega_d^4 \\ +4\,\zeta_d^2\omega_b^6\omega_s^2\omega_d^2 - \mu_1\,\mu_2\,\omega_s^6\omega_d^4 + 3\,\mu_2^2\omega_b^2\omega_s^4\omega_d^4 + \mu_2^2\omega_s^6\omega_d^4 \\ +4\,\mu_1\,\omega_b^6\omega_d^4 + 3\,\mu_2\,\omega_b^4\omega_s^4\omega_d^2 - 4\,\zeta_d^2\omega_b^4\omega_s^4\omega_d^2 - 3\,\mu_1\,\omega_b^6\omega_s^2\omega_d^2 \\ +3\,\mu_1^2\omega_b^4\omega_s^2\omega_d^4 - 4\,\mu_2\,\omega_b^4\omega_s^2\omega_d^4 + \omega_b^6\omega_s^4 - 2\,\omega_b^6\omega_s^2\omega_d^2 \\ +\omega_b^6\omega_d^4 - \omega_b^4\omega_s^6 + 2\,\omega_b^4\omega_s^4\omega_d^2 - \omega_b^4\omega_s^2\omega_d^4 - \mu_1^3\mu_2\,\omega_b^4\omega_s^2\omega_d^4 \end{array}\right)}{2\,\omega_b^4\omega_d\zeta_d\left(\mu_1\,\omega_b^2 - \mu_2\,\omega_s^2\right)\omega_s^6} \tag{25}$$

Eq. (25) is partially differentiated by ζ_d and ω_d. Therefore, the mathematical expressions for differentiation have been derived as

$$\frac{\partial\sigma_{x_s}^2}{\partial\zeta_d} = 0 \quad \text{and} \quad \frac{\partial\sigma_{x_s}^2}{\partial\omega_d} = 0 \tag{26}$$

Eq. (25) has been substituted in the first expression of Eq. (26). Therefore, the closed-form expression for damping ratio of the novel tuned mass dampers has been derived as

$$\zeta_d=\sqrt{\frac{\begin{array}{c}\mu_1^4\omega_b^6\omega_d^4-\mu_1^3\mu_2\,\omega_b^4\omega_s^2\omega_d^4+\mu_1^3\omega_b^6\omega_s^2\omega_d^2+4\,\mu_1^3\omega_b^6\omega_d^4\\+2\,\mu_1^3\omega_b^4\omega_s^2\omega_d^4-\mu_1^2\mu_2\,\omega_b^4\omega_s^4\omega_d^2-6\,\mu_1^2\mu_2\,\omega_b^4\omega_s^2\omega_d^4\\-2\,\mu_1^2\mu_2\,\omega_b^2\omega_s^4\omega_d^4+2\,\mu_1\,\mu_2^2\omega_b^2\omega_s^4\omega_d^4+6\,\mu_1^2\omega_b^6\omega_d^4\\+3\,\mu_1^2\omega_b^4\omega_s^2\omega_d^4+\mu_1^2\omega_b^2\omega_s^4\omega_d^4-9\,\mu_1\,\mu_2\,\omega_b^4\omega_s^2\omega_d^4\\-4\,\mu_1\,\mu_2\,\omega_b^2\omega_s^4\omega_d^4-\mu_1\,\mu_2\,\omega_s^6\omega_d^4+3\,\mu_2^2\omega_b^2\omega_s^4\omega_d^4\\-3\,\mu_1\,\omega_b^6\omega_s^2\omega_d^2+4\,\mu_1\,\omega_b^6\omega_d^4+3\,\mu_2\,\omega_b^4\omega_s^4\omega_d^2\\+\mu_2^2\omega_s^6\omega_d^4-4\,\mu_2\,\omega_b^4\omega_s^2\omega_d^4+\omega_b^6\omega_s^4-2\,\omega_b^6\omega_s^2\omega_d^2\\+\omega_b^6\omega_d^4-\omega_b^4\omega_s^6+2\,\omega_b^4\omega_s^4\omega_d^2-\omega_b^4\omega_s^2\omega_d^4\end{array}}{\begin{array}{c}4\,\mu_1^3\omega_b^6\omega_s^2\omega_d^2-4\,\mu_1^2\mu_2\,\omega_b^4\omega_s^4\omega_d^2+12\,\mu_1^2\omega_b^6\omega_s^2\omega_d^2\\+4\,\mu_1^2\omega_b^4\omega_s^4\omega_d^2-16\,\mu_1\,\mu_2\,\omega_b^4\omega_s^4\omega_d^2-4\,\mu_1\,\mu_2\,\omega_b^2\omega_s^6\omega_d^2\\+4\,\mu_2^2\omega_b^2\omega_s^6\omega_d^2+12\,\mu_1\,\omega_b^6\omega_s^2\omega_d^2-12\,\mu_2\,\omega_b^4\omega_s^4\omega_d^2\\+4\,\omega_b^6\omega_s^2\omega_d^2-4\,\omega_b^4\omega_s^4\omega_d^2\end{array}}} \tag{27}$$

Eq. (27) substitutes in Eq. (25) and a modified expression for Eq. (25) has been obtained which substitutes in the second expression of Eq. (26). Therefore, the closed-form expression for optimal frequency of the novel tuned mass dampers has been derived as

$$(\omega_d)_{opt}=\sqrt{\frac{\begin{array}{c}\omega_b^6(3\,\mu_1\,\omega_s^2+2\,\omega_s^2-\mu_1^3\omega_s^2)\\+\omega_b^4(\mu_1^2\mu_2\,\omega_s^4-3\,\mu_2\,\omega_s^4-2\,\omega_s^4)\end{array}}{\begin{array}{c}\omega_b^6(2\,\mu_1^4+8\,\mu_1^3+12\,\mu_1^2+8\,\mu_1\,+2\,)\\+\omega_b^4(-2\,\mu_1^3\mu_2\,\omega_s^2+4\,\mu_1^3\omega_s^2-12\,\mu_1^2\mu_2\,\omega_s^2)\\+\omega_b^4(6\,\mu_1^2\omega_s^2-18\,\mu_1\,\mu_2\,\omega_s^2-8\,\mu_2\,\omega_s^2-2\,\omega_s^2)\\+\omega_b^2(-4\,\mu_1^2\mu_2\,\omega_s^4+4\,\mu_1\,\mu_2^2\omega_s^4+2\,\mu_1^2\omega_s^4)\\+\omega_b^2(-8\,\mu_1\,\mu_2\,\omega_s^4+6\,\mu_2^2\omega_s^4)\\+2\,\mu_2^2\omega_s^6-2\,\mu_1\,\mu_2\,\omega_s^6\end{array}}} \tag{28}$$

Eq. (28) has been non-dimensionalized and listed in Appendix B. Now, Eq. (28) substitutes in Eq. (27) and the closed-form expressions for the optimal viscous damping ratio of the novel tuned mass dampers have been derived as

$$(\zeta_d)_{opt}=\sqrt{\frac{(\mu_1\,\omega_b^2-\mu_2\,\omega_s^2)\left(\begin{array}{c}\omega_b^6(20\,\mu_1^2-\mu_1^5+10\,\mu_1^3+15\,\mu_1\,+4)\\+\omega_b^4(\mu_1^4\mu_2\,\omega_s^2-4\,\mu_1^3\omega_s^2-6\,\mu_1^2\mu_2\,\omega_s^2)\\+\omega_b^4(-12\,\mu_1^2\omega_s^2-8\,\mu_1\,\mu_2\,\omega_s^2-12\,\mu_1\,\omega_s^2)\\+\omega_b^4(-3\,\mu_2\,\omega_s^2-4\,\omega_s^2)\\+\omega_b^2(-8\,\mu_1^2\omega_s^4+8\,\mu_1\,\mu_2\,\omega_s^4-8\,\mu_1\,\omega_s^4)\\+8\,\mu_2\,\omega_b^2\omega_s^4-4\,\mu_1\,\omega_s^6+4\,\mu_2\,\omega_s^6\end{array}\right)}{\begin{array}{c}8\,\omega_b^2\left(3\,\mu_1\,\omega_b^2+2\,\omega_b^2-\mu_1^3\omega_b^2+\mu_1^2\mu_2\,\omega_s^2-3\,\mu_2\,\omega_s^2-2\,\omega_s^2\right)\\\left(\begin{array}{c}\omega_b^4(\mu_1^3+3\,\mu_1^2+3\,\mu_1\,+1)\\+\omega_b^2(-\mu_1^2\mu_2\,\omega_s^2+\mu_1^2\omega_s^2-4\,\mu_1\,\mu_2\,\omega_s^2-3\,\mu_2\,\omega_s^2-\omega_s^2)\\-\mu_2\,\omega_s^4\mu_1+\mu_2^2\omega_s^4\end{array}\right)\end{array}}} \tag{29}$$

Eq. (29) has been non-dimensionalized and listed in Appendix B.

2.6. H_∞ optimization for novel tuned mass dampers

H_∞ optimization technique has been applied to minimize the maximum dynamic responses of the primary structures controlled by novel tuned mass dampers and the exact closed-form expressions for optimized system parameters for novel tuned mass dampers have been obtained. Hence, Eq. (14) has been non-dimensionalized and expressed as

$$\begin{bmatrix}\frac{(\mu_2\,\eta^2-\mu_1\,\eta_b^2)(2\,i\eta\,\zeta_d\,\eta_d-\eta^2+\eta_d^2)}{\eta^2-\eta_b^2} & -\frac{\eta^2(\mu_2\,\eta^2-\mu_1\,\eta_b^2)}{\eta^2-\eta_b^2}\\ -\frac{\eta_d(\mu_2\,\eta^2-\mu_1\,\eta_b^2)(2\,i\eta\,\zeta_d+\eta_d)}{\eta^2-\eta_b^2} & -\eta^2+1+2\,i\zeta_s\,\eta\end{bmatrix}\begin{Bmatrix}X_d\\X_s\end{Bmatrix}=-\begin{bmatrix}\mu_{ad}\\1\end{bmatrix}\frac{A_g}{\omega_s^2} \tag{30}$$

where $\eta=\omega/\omega_s$, $\mu_{ad}=(\mu_1\,\eta_b^2-\eta^2\mu_2)/(\eta_b^2-\eta^2)$, and the details of other system parameters have already illustrated in previous section. The dynamic response of SDOF system has been derived as

$$H_s(\eta)=\frac{X_s}{A_g}\omega_s^2=\frac{\left(\begin{array}{c}\eta^2\mu_2\,\eta_d^2-\eta_b^2\mu_1\,\eta_d^2-\eta^4+\eta^2\eta_b^2+\eta^2\eta_d^2-\eta_b^2\eta_d^2\\+2\mathrm{i}\,\zeta_d\,\eta_d\eta\left((\mu_2+1)\eta^2-(\mu_1+1)\eta_b^2\right)\end{array}\right)}{\Delta_n} \tag{31}$$

Δ_n has been derived as

$$\Delta_n = \begin{matrix} \eta^4\mu_2\,\eta_d{}^2 + 4\,\eta^4\zeta_d\,\zeta_s\,\eta_d - \eta^2\eta_b{}^2\mu_1\,\eta_d{}^2 - 4\,\eta^2\eta_b{}^2\zeta_d\,\zeta_s\,\eta_d - \eta^6 \\ +\eta^4\eta_b{}^2 + \eta^4\eta_d{}^2 - \eta^2\eta_b{}^2\eta_d{}^2 + \eta^4 - \eta^2\eta_b{}^2 - \eta^2\eta_d{}^2 + \eta_b{}^2\eta_d{}^2 \\ +\mathrm{i}\begin{pmatrix} 2\,\eta^5\mu_2\,\zeta_d\,\eta_d - 2\,\eta^3\eta_b{}^2\mu_1\,\zeta_d\,\eta_d + 2\,\eta^5\zeta_d\,\eta_d - 2\,\eta^3\eta_b{}^2\zeta_d\,\eta_d + 2\,\eta^5\zeta_s \\ -2\,\eta^3\eta_b{}^2\zeta_s - 2\,\eta^3\zeta_s\,\eta_d{}^2 + 2\,\eta\,\eta_b{}^2\zeta_s\,\eta_d{}^2 - 2\,\eta^3\zeta_d\,\eta_d + 2\,\eta\,\eta_b{}^2\zeta_d\,\eta_d \end{pmatrix} \end{matrix} \tag{32}$$

After considering $\zeta_s = 0$. The modulus of the dynamic response of the primary structure has been derived as

$$|H_s(\eta)| = \sqrt{\frac{A^2 + \zeta_d^2 B^2}{C^2 + \zeta_d^2 D^2}} = \left|\frac{B}{D}\right| \sqrt{\frac{\left(\frac{A}{B}\right)^2 + \zeta_d^2}{\left(\frac{C}{D}\right)^2 + \zeta_d^2}} \tag{33}$$

where

$$\begin{aligned} A &= \eta^2\mu_2\,\eta_d{}^2 - \eta_b{}^2\eta_d{}^2\mu_1 - \eta^4 + \eta^2\eta_b{}^2 + \eta^2\eta_d{}^2 - \eta_b{}^2\eta_d{}^2 \\ B &= 2\,\eta_d\zeta_d\,\eta^3\mu_2 - 2\,\eta\,\eta_b{}^2\mu_1\,\zeta_d\,\eta_d + 2\,\eta^3\zeta_d\,\eta_d - 2\,\eta\,\eta_b{}^2\zeta_d\,\eta_d \\ C &= \begin{matrix} \eta^4\mu_2\,\eta_d{}^2 - \eta^2\eta_b{}^2\mu_1\,\eta_d{}^2 - \eta^6 + \eta^4\eta_b{}^2 + \eta^4\eta_d{}^2 \\ -\eta^2\eta_b{}^2\eta_d{}^2 + \eta^4 - \eta^2\eta_b{}^2 - \eta^2\eta_d{}^2 + \eta_b{}^2\eta_d{}^2 \end{matrix} \\ D &= \begin{matrix} 2\,\eta^5\mu_2\,\zeta_d\,\eta_d - 2\,\eta^3\eta_b{}^2\mu_1\,\zeta_d\,\eta_d + 2\,\eta^5\zeta_d\,\eta_d \\ -2\,\eta^3\eta_b{}^2\zeta_d\,\eta_d - 2\,\eta^3\zeta_d\,\eta_d + 2\,\eta\,\eta_b{}^2\zeta_d\,\eta_d \end{matrix} \end{aligned} \tag{34}$$

Now, applying the fixed-point theory [7,11,16], two constraints have been derived which are listed below.

$$\left(\frac{A}{B}\right)^2\bigg|_{\eta_j} = \left(\frac{C}{D}\right)^2\bigg|_{\eta_j} \quad \text{and} \quad \left(\frac{B}{D}\right)^2\bigg|_{\eta_1} = \left(\frac{B}{D}\right)^2\bigg|_{\eta_2} \tag{35}$$

After applying the first constraints of Eq. (35), a polynomial equation has been derived which is expressed as

$$\begin{matrix} \eta^6 + \left(-\mu_2\,\eta_d{}^2 - \eta_b{}^2 - \eta_d{}^2 - 1\right)\eta^4 \\ +\left(\eta_b{}^2\mu_1\,\eta_d{}^2 + \eta_b{}^2\eta_d{}^2 + \eta_b{}^2 + \eta_d{}^2\right)\eta^2 - \eta_b{}^2\eta_d{}^2 \end{matrix} = 0 \tag{36}$$

It has been considered that $\eta_3 > \eta_2 > \eta_1$. Therefore, the mathematical relation between roots have been derived as [96]:

$$\eta_1^2 + \eta_2^2 + \eta_3^2 = \mu_2\,\eta_d{}^2 + \eta_b{}^2 + \eta_d{}^2 + 1 \tag{37}$$

$$\eta_2{}^2\eta_1{}^2 + \eta_3{}^2\eta_1{}^2 + \eta_2{}^2\eta_3{}^2 = \eta_b{}^2\mu_1\,\eta_d{}^2 + \eta_b{}^2\eta_d{}^2 + \eta_b{}^2 + \eta_d{}^2 \tag{38}$$

$$\eta_1{}^2\eta_2{}^2\eta_3{}^2 = \eta_b{}^2\eta_d{}^2 \tag{39}$$

Now, using the second constraints of Eq. (35), the closed-form expression for deriving η_1^2 and η_2^2 has been derived as

$$\eta_1{}^2 + \eta_2{}^2 = 2 \tag{40}$$

where, the roots of polynomial equations have been derived as η_N^2 terms where $N = 1, 2, 3, 4, 5, 6$. The values of multiplication of roots have been neglected by considering $\eta_1^{j+2}\eta_2^{j+2} \neq 0$, where $j = 1, 2, 3, 4, \ldots.\infty$. using Eqs. (37) and (40), the closed-form equations for η_3^2 has been derived and expressed as

$$\eta_3^2 = \eta_d{}^2\mu_2 + \eta_b{}^2 + \eta_d{}^2 - 1 \tag{41}$$

Eq. (41) inserts in Eqs. (38) and (39) and a equation has been derived as

$$\begin{matrix} \left(\eta_b{}^2\mu_1\,\mu_2 + \eta_b{}^2\mu_1 + \eta_b{}^2\mu_2 + \eta_b{}^2 - 2\,\mu_2{}^2 - 3\,\mu_2 - 1\right)\eta_d{}^4 \\ +\left(\eta_b{}^4\mu_1 + \eta_b{}^4 - \eta_b{}^2\mu_1 - 3\,\eta_b{}^2\mu_2 - 4\,\eta_b{}^2 + 4\,\mu_2 + 3\right)\eta_d{}^2 \\ -\eta_b{}^4 + 3\,\eta_b{}^2 - 2 \end{matrix} = 0 \tag{42}$$

The exact closed-form expression for optimized frequency ratio for novel tuned mass dampers is derived from Eq. (42) and expressed as

$$(\eta_d)_{opt}^2 = \frac{\left(\begin{matrix} -\eta_b{}^4\mu_1 - \eta_b{}^4 + \eta_b{}^2\mu_1 + 3\,\eta_b{}^2\mu_2 + 4\,\eta_b{}^2 - 4\,\mu_2 - 3 \\ + \sqrt{\begin{pmatrix} \eta_b^8\mu_1{}^2 + 2\,\eta_b{}^8\mu_1 + \eta_b{}^8 - 2\,\eta_b{}^6\mu_1{}^2 - 2\,\eta_b{}^6\mu_1\,\mu_2 \\ -6\,\eta_b{}^6\mu_1 - 2\,\eta_b{}^6\mu_2 - 4\,\eta_b{}^6 + \eta_b{}^4\mu_1{}^2 + 2\,\eta_b{}^4\mu_1\,\mu_2 \\ +\eta_b{}^4\mu_2{}^2 + 2\,\eta_b{}^4\mu_1 + 8\,\eta_b{}^4\mu_2 + 6\,\eta_b{}^4 + 2\,\eta_b{}^2\mu_1 \\ -6\,\eta_b{}^2\mu_2 - 4\,\eta_b{}^2 + 1 \end{pmatrix}} \end{matrix} \right)}{2\,\eta_b{}^2\mu_1\,\mu_2 + 2\,\eta_b{}^2\mu_1 + 2\,\eta_b{}^2\mu_2 + 2\,\eta_b{}^2 - 4\,\mu_2{}^2 - 6\,\mu_2 - 2} \tag{43}$$

Now, $\eta_{1,2}^2$ has been derived as

$$\eta_{1,2}^2 = 1 \pm \sqrt{\eta_b{}^2 + \eta_d{}^2 - \eta_b{}^2\mu_1\,\eta_d{}^2 - \eta_b{}^2\eta_d{}^2 + 2\,\mu_2\,\eta_d{}^2 - 1} \tag{44}$$

The exact closed-form expression for optimal ζ_d derives using the mathematical formulation below.

$$\left.\frac{\partial |H_s(\eta)|^2}{\partial \eta^2}\right|_{\eta^2_{1,2}} = 0 \quad \text{and} \quad (\zeta_d)_{opt} = \sqrt{\frac{\zeta_{d1}^2 + \zeta_{d2}^2}{2}} \tag{45}$$

As a result, the exact closed-form expression for optimal $(\zeta_{d1,d2})^2{}_{opt}$ derives as

$$(\zeta_{d1,d2})^2{}_{opt} = \frac{\left(\begin{array}{c} -\eta^{12}_{1,2} + \left(2\,\mu_2\,\eta_d{}^2 + 2\,\eta_b{}^2 + 2\,\eta_d{}^2 + 2\right)\eta^{10}_{1,2} \\ +\begin{pmatrix} -\mu_2{}^2\eta_d{}^4 - 2\,\eta_b{}^2\mu_1\,\eta_d{}^2 - 2\,\eta_b{}^2\mu_2\,\eta_d{}^2 \\ -2\,\mu_2\,\eta_d{}^4 - \eta_b{}^4 - 4\,\eta_b{}^2\eta_d{}^2 - \eta_d{}^4 \\ -2\,\mu_2\,\eta_d{}^2 - 4\,\eta_b{}^2 - 4\,\eta_d{}^2 - 1 \end{pmatrix}\eta^8_{1,2} \\ +\begin{pmatrix} 2\,\eta_b{}^2\mu_1\,\mu_2\,\eta_d{}^4 + 2\,\eta_b{}^4\mu_1\,\eta_d{}^2 + 2\,\eta_b{}^2\mu_1\,\eta_d{}^4 \\ +2\,\eta_b{}^2\mu_2\,\eta_d{}^4 + 2\,\eta_b{}^4\eta_d{}^2 + 2\,\eta_b{}^2\eta_d{}^4 + 2\,\eta_d{}^2 \\ +2\,\eta_b{}^2\mu_1\,\eta_d{}^2 + 2\,\eta_b{}^2\mu_2\,\eta_d{}^2 + 2\,\mu_2\,\eta_d{}^4 \\ +2\,\eta_b{}^4 + 8\,\eta_b{}^2\eta_d{}^2 + 2\,\eta_d{}^4 + 2\,\eta_b{}^2 \end{pmatrix}\eta^6_{1,2} \\ +\begin{pmatrix} -\eta_b{}^4\mu_1{}^2\eta_d{}^4 - 2\,\eta_b{}^4\mu_1\,\eta_d{}^4 - \eta_b{}^4\eta_d{}^4 - \eta_d{}^4 \\ -2\,\eta_b{}^4\mu_1\,\eta_d{}^2 - 2\,\eta_b{}^2\mu_1\,\eta_d{}^4 - 2\,\eta_b{}^2\mu_2\,\eta_d{}^4 \\ -4\,\eta_b{}^4\eta_d{}^2 - 4\,\eta_b{}^2\eta_d{}^4 - \eta_b{}^4 - 4\,\eta_b{}^2\eta_d{}^2 \end{pmatrix}\eta^4_{1,2} \\ +\left(2\,\eta_b{}^4\mu_1\,\eta_d{}^4 + 2\,\eta_b{}^4\eta_d{}^4 + 2\,\eta_b{}^4\eta_d{}^2 + 2\,\eta_b{}^2\eta_d{}^4\right)\eta^2_{1,2} \\ -\eta_b{}^4\eta_d{}^4 \end{array}\right)}{\left(\begin{array}{c} \left(4\,\mu_2{}^2\eta_d{}^2 + 8\,\mu_2\,\eta_d{}^2 + 4\,\eta_d{}^2\right)\eta^{10}_{1,2} \\ +\begin{pmatrix} -8\,\eta_b{}^2\mu_1\,\mu_2\,\eta_d{}^2 - 8\,\eta_b{}^2\mu_1\,\eta_d{}^2 - 8\,\eta_d{}^2 \\ -8\,\eta_b{}^2\mu_2\,\eta_d{}^2 - 8\,\eta_b{}^2\eta_d{}^2 - 8\,\mu_2\,\eta_d{}^2 \end{pmatrix}\eta^8_{1,2} \\ +\begin{pmatrix} 4\,\eta_b{}^4\mu_1{}^2\eta_d{}^2 + 8\,\eta_b{}^4\mu_1\,\eta_d{}^2 + 4\,\eta_b{}^4\eta_d{}^2 + 4\,\eta_d{}^2 \\ +8\,\eta_b{}^2\mu_1\,\eta_d{}^2 + 8\,\eta_b{}^2\mu_2\,\eta_d{}^2 + 16\,\eta_b{}^2\eta_d{}^2 \end{pmatrix}\eta^6_{1,2} \\ +\left(-8\,\eta_b{}^4\mu_1\,\eta_d{}^2 - 8\,\eta_b{}^4\eta_d{}^2 - 8\,\eta_b{}^2\eta_d{}^2\right)\eta^4_{1,2} \\ +4\,\eta_d{}^2\eta^2_{1,2}\eta_b{}^4 \end{array}\right)} \tag{46}$$

Eq. (44) has been inserted in Eq. (46) and the second equation of Eq. (45) to obtain exact values of optimal viscous damping of novel tuned mass dampers.

3. Results and discussion

3.1. Effective mass and stiffness

Eqs. (19) and (20) are applied to identify the effect of negative stiffness inertial amplifier on the static system properties of the novel tuned mass dampers. The contour diagram of μ_{fs} as a function of α and θ has been displayed in Fig. 2(a). Overall result shows that the static effective mass ratio μ_{fs} has only contained the effect of the inertial amplifier; mass amplification occurs at lower values of inertial angle θ. This figure also shows that adequate mass amplification occurs at $\theta \leq 30^\circ$. Hence, these values of inertial angle have been acknowledged as the critical angles for the novel tuned mass dampers. The maximum amount of mass amplification occurs at $\theta \leq 14^\circ$. This mass amplification at a lower angle significantly increases the effective damping of the novel tuned mass damper, which helps to dissipate the energy of the controlled structures during vibration. Therefore, lower values of inertial angles (i.e., $\theta \leq 14^\circ$) have been recommended for designing these novel dampers. Hence, $\theta = 14^\circ$ has been applied throughout the paper for determining the results.

The maximum mass amplification occurs for higher values of α, which defines the ratio of total vertical mass to the total static mass of the novel tuned mass dampers, implying that the static effective mass increases when α increases. For better understanding, if the value of μ_T considers as 0.01, then the value of α only depends upon the static mass of novel dampers, i.e., $\mu_d + 2\mu_T$ which implies lower static mass provides more static mass amplifications than the higher static mass.

Furthermore, the effectiveness of the negative stiffness inertial amplifier on the static masses of the novel tuned mas dampers has been observed in Fig. 2(b), where the contour diagram of the dynamic effective mass (μ_f) as a function of μ and η/η_b has been observed to the system's resonating frequency regions. $\alpha = 0.20$ and $\theta = 14^\circ$ are applied for this graph. Precisely, at $1.01 \leq \eta/\eta_b \leq 1.96$ and for $\mu = 0$ which represents the (NS-TMD). The effectiveness of the inertial amplifier tends to zero for NS-TMD at that particular frequency region. Hence, It has been proved that the vertical spring-mass system attached to the amplifier's mass produces dynamic negative masses near resonance frequency efficiently, and these spring-mass systems exactly behave as negative stiffness devices. For $\mu > 0$, the presence of dynamic negative masses decreases and becomes zero at $\mu = 1.0$. $0.1 \leq \mu \leq 0.5$ represents the NSIA-TMD with higher values of dynamic negative masses, whereas $0.6 \leq \mu \leq 0.9$ represents the NSIA-TMD with lower values of dynamic negative masses near resonating frequency region. $\mu = 1.0$ represents IA-TMD and zero negative masses are observed in the overall frequency region; only the mass amplifications occur for this particular system. The significant amount of mass amplifications are occurred at

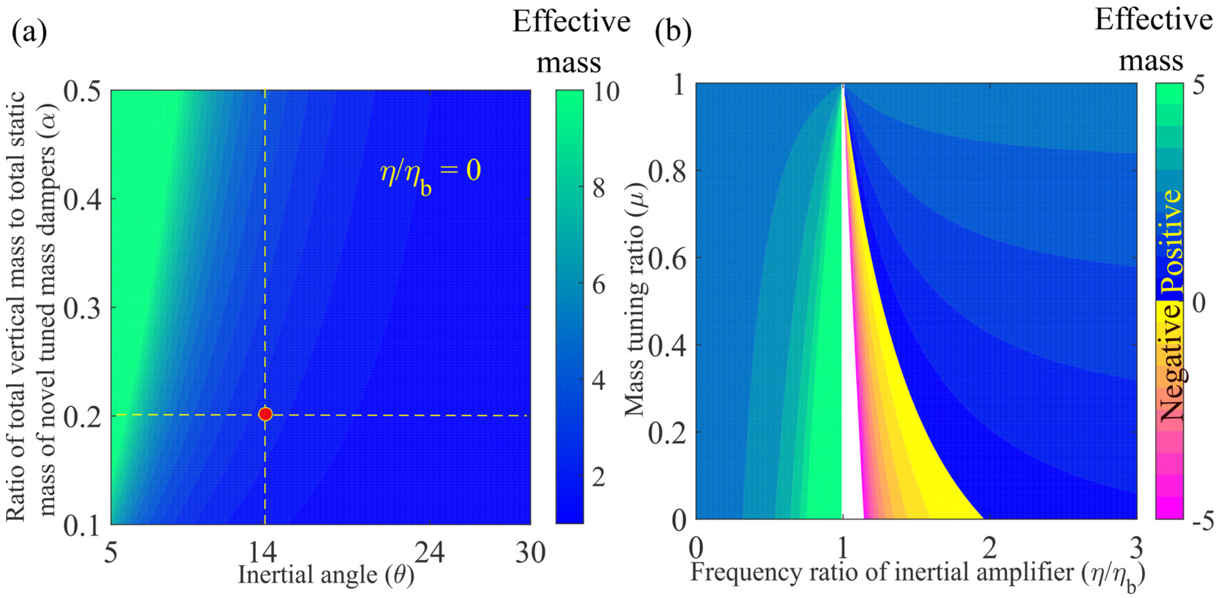

Fig. 2. (a) The contour diagram of μ_{sf} as a function of α and θ and (b) the contour diagram of μ_f as a function of μ and η/η_b have been displayed.

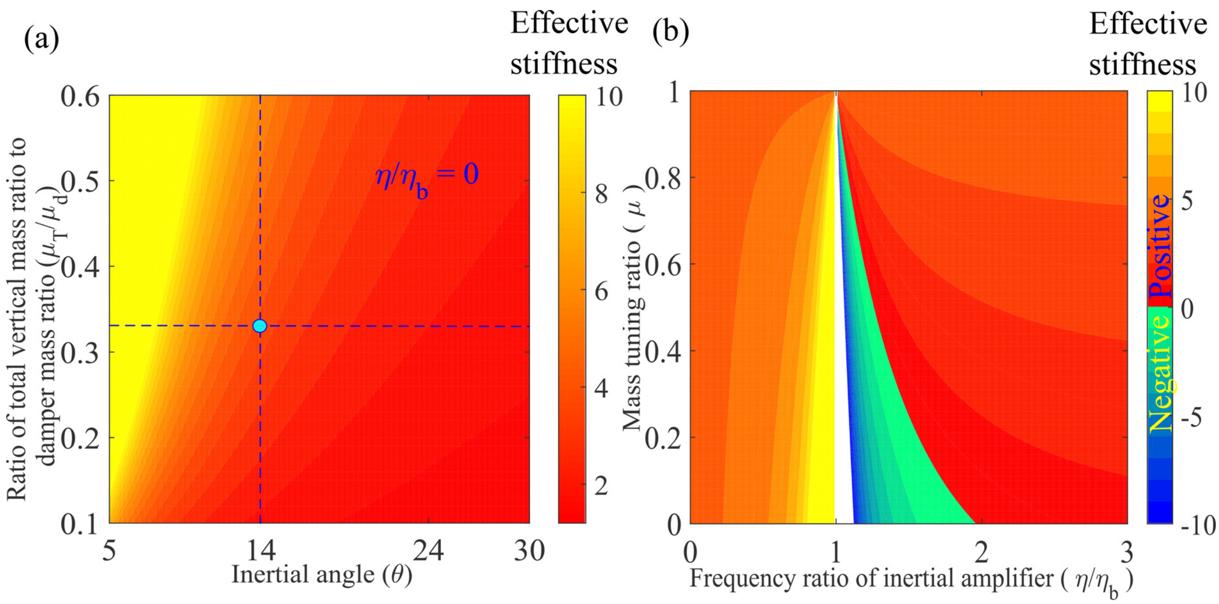

Fig. 3. (a) The contour diagram of κ_{fs} as a function of (μ_T/μ_d) and θ and (b) the contour diagram of (κ_f) as a function of μ and η/η_b have been displayed.

$\eta/\eta_b > 1.96$, which provides enhanced effective mass to the IA-TMD without adding any static masses. Therefore, the significant amount of dynamic negative masses are observed for NS-TMD ($\mu = 0$) and NSIA-TMD ($0.1 \leq \mu \leq 0.9$), whereas the significant amount of positive effective masses is observed for IA-TMD ($\mu = 1$) which influences the dynamic effective stiffness of the novel tuned mass dampers simultaneously.

Eqs. (22) and (23) are applied to identify the effect of negative stiffness inertial amplifiers on the static stiffness of the novel tuned mass dampers. The contour diagram of κ_{fs} as a function of μ_T/μ_d and θ has been displayed in Fig. 3(a). The static effective stiffness ratio κ_{fs} has only contained positive effective stiffness with higher values at lower values of inertial angle θ. Basically, the effective stiffness of novel dampers increases when the inertial angle decreases. In fact, the larger positive effective stiffness provided by the novel dampers enhances the dampers' restoring forces and has potentially reduced the deflections of the primary dynamic systems during vibration. This figure also shows that adequate stiffness amplification occurs at $\theta \leq 30^\circ$. Hence, these values of inertial angle have been verified again and acknowledged as the critical angles for the novel tuned mass dampers. For $\theta \leq 14^\circ$, the effective stiffness amplifications are appeared the most

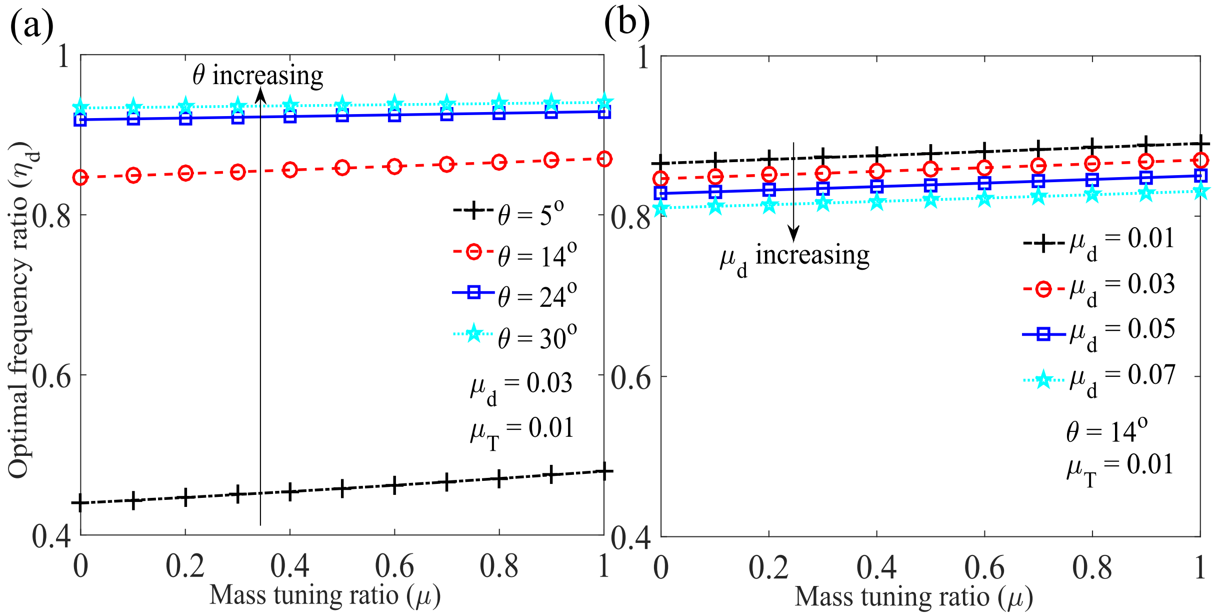

Fig. 4. The variations of optimal frequency ratio η_d versus mass tuning ratio μ for different values of (a) inertial angle θ and (b) damper mass ratio μ_d of novel tuned mass dampers.

and these values for inertial angles are recommended to achieve robust dynamic response reduction capacity for novel tuned mass dampers. Another observations, the maximum positive effective stiffness amplification occurs for higher values of μ_T/μ_d, implying that the static effective stiffness increases when μ_T/μ_d increases.

In addition, the effectiveness of the negative stiffness inertial amplifiers on the static stiffness of the novel tuned mass dampers have been observed in Fig. 3(b), where the contour diagram of the dynamic effective stiffness (κ_f) as a function of μ and η/η_b has been observed to the system's resonating frequency regions. $\mu_T/\mu_d = 0.33$ and $\theta = 14^\circ$ are applied for this graph. The positive dynamic effective stiffness amplifications are observed at $0 \leq \eta/\eta_b \leq 0.99$ whereas the negative dynamic effective stiffness is located at $1.01 \leq \eta/\eta_b \leq 1.96$ for NS-TMD ($\mu = 0$). Therefore, the negative dynamic system properties are only observed at near resonating frequencies for NS-TMD where the inertial amplifiers' effect is null. It has also been crosschecked and verified that the vertical spring-mass system attached to the amplifier's mass produces dynamic negative masses near resonance frequency efficiently, and these spring-mass systems exactly worked as negative stiffness devices. These dynamic negative stiffness lessen the frequency of the dampers, providing higher dynamic effective damping to the novel tuned mass damper, which significantly contributes to dissipating the energy of the controlled dynamic systems. Overall results showed that these negative stiffness inertial amplifiers-based tuned mass dampers increase traditional tuned mass dampers' dynamic response reduction capacity through higher energy dissipation, giving more restoring forces and damping forces reduction simultaneously sufficient load-bearing capacity to the controlled dynamic systems. For $\mu > 0$, the presence of dynamic negative stiffness decreases and becomes zero at $\mu = 1.0$. $0.1 \leq \mu \leq 0.5$ represents the NSIA-TMD with higher values of dynamic negative stiffness, whereas $0.6 \leq \mu \leq 0.9$ represents the NSIA-TMD with lower values of dynamic negative stiffness near resonating frequency region. $\mu = 1.0$ represents IA-TMD and zero negative stiffness is observed in the overall frequency region; only the mass amplifications and slight stiffness amplifications occur for this system. The significant amount of mass amplifications and slight stiffness amplifications occurred at $\eta/\eta_b > 1.96$, which provides enhanced effective mass to the IA-TMD without adding any static masses. Therefore, the significant amount of dynamic negative stiffness is observed for NS-TMD ($\mu = 0$) and NSIA-TMD ($0.1 \leq \mu \leq 0.9$), whereas a notable amount of positive effective stiffness is observed for IA-TMD ($\mu = 1$) which influences the dynamic effective stiffness of the novel tuned mass dampers during vibration. Therefore, the negative stiffness inertial amplifiers based tuned mass dampers increase the dynamic response reduction capacity of traditional tuned mass dampers through higher energy dissipation, giving more restoring forces and damping forces reductions simultaneously sufficient load-bearing capacity to the controlled dynamic systems.

3.2. H_2 optimization

The variations of η_d versus μ for different values of θ are displayed in Fig. 4(a). The black ($\theta = 5^\circ$), red ($\theta = 14^\circ$), blue ($\theta = 24^\circ$), and cyan ($\theta = 30^\circ$) lines with markers are applied to identify each plot. The system parameters are considered as $\mu_T = 0.01$ and $\mu_d = 0.03$. The optimal frequency ratio of novel tuned mass dampers increases as the inertial angle of the amplifier increases. Thus, the natural frequency of novel tuned mass dampers increases, as do the restoring forces, possibly reducing primary dynamic system deflections during vibration. The inverse effect occurs as the damper mass ratio increases.

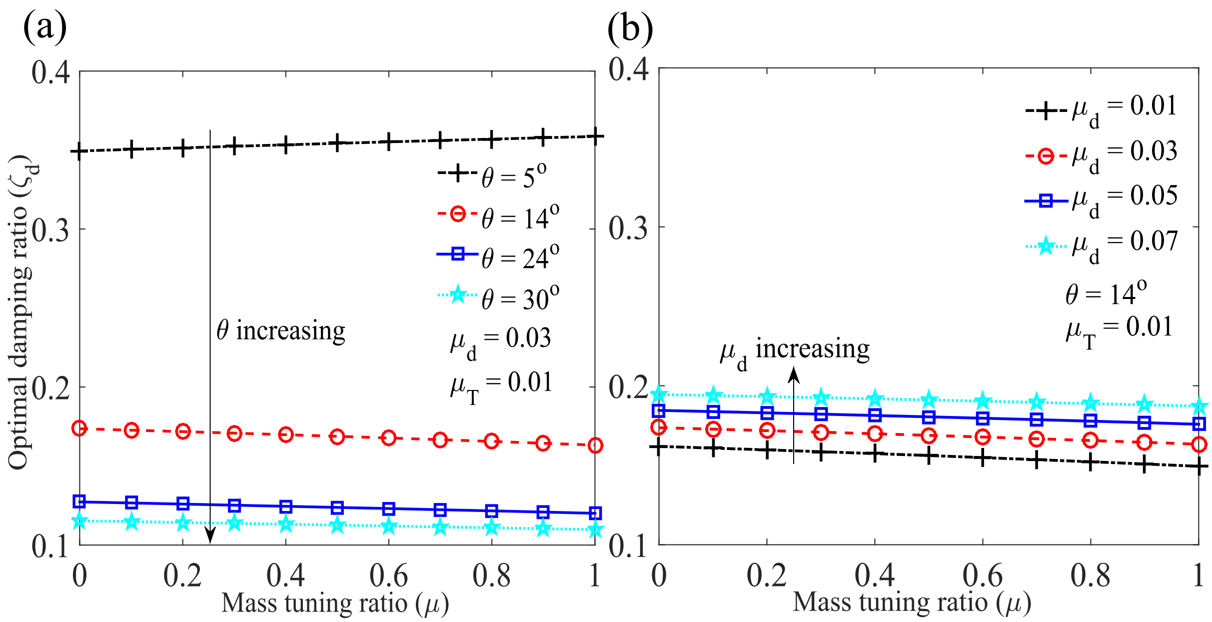

Fig. 5. The variations of optimal viscous damping ratio ζ_d versus mass tuning ratio μ for different values of (a) inertial angle θ and (b) damper mass ratio μ_d of novel tuned mass dampers.

The variations of optimal frequency ratio η_d versus mass tuning ratio μ of the novel tuned mass dampers for the different values of damper mass ratio μ_d have been displayed in Fig. 4(b). The black ($\mu_d = 0.01$), red ($\mu_d = 0.03$), blue ($\mu_d = 0.05$), and cyan ($\mu_d = 0.07$) lines with markers are applied to identify each plot. The system parameters are considered as $\mu_T = 0.01$ and $\theta = 14^\circ$. The optimal frequency ratio increases as the mass tuning ratio of the novel tuned mass dampers increase and decreases as the damper mass ratio increases. Therefore, the natural frequency of the novel tuned mass dampers decreases, whereas the structure's time period increases, potentially reducing primary dynamic system deflections during vibration. For both Fig. 4(a) and (b), the optimal frequency ratio increases as the mass tuning ratio increases. Thus, the natural frequency of the novel tuned mass dampers decreases, as do the restoring forces, possibly reducing the primary dynamic system's deflections during vibration.

The variations of optimal damping ratio ζ_d versus mass tuning ratio μ of the novel tuned mass dampers for the different values of inertial angle θ have been displayed in Fig. 5(a). The black ($\theta = 5^\circ$), red ($\theta = 14^\circ$), blue ($\theta = 24^\circ$), and cyan ($\theta = 30^\circ$) lines with markers are applied to identify each plot. For this graph, other system parameters are considered as $\mu_T = 0.01$ and $\mu_d = 0.03$. The optimal damping ratio of the novel tuned mass dampers decreases as the mass tuning ratio and inertial angle increase. Thus, the damping increases at a lower damping ratio for IA-TMD and slightly higher for NS-TMD and NSIA-TMD, as does the damping force reduction capacity, possibly reducing the primary dynamic system's deflections during vibration effectively. In contrast, the damping ratio increases as the damper mass ratio increases, which has been observed from Fig. 5(b).

The black ($\mu_d = 0.01$), red ($\mu_d = 0.03$), blue ($\mu_d = 0.05$), and cyan ($\mu_d = 0.07$) lines with markers are applied to identify each plot. The system parameters are considered as $\mu_T = 0.10$ and $\theta = 14^\circ$.

As the damper mass ratio increases, the optimal damping ratio also increases. Thus, a higher damper mass ratio provides additional damping force reduction capacity, enabling these dampers to surpass conventional tuned mass dampers in terms of response reduction capacity.

The optimal damping ratio for Fig. 5(a) decreases as the inertial angle decreases. The damping ratio increases at $\theta = 5^\circ$ according to the mass tuning ratio. However, when the inertial angle increases, this characteristic changes. When $\theta \geq 10^\circ$ is increased, the optimal damping ratio decreases. Fig. 5(b) provides a smooth transition between mass tuning ratio and optimal damping ratio. For each value of damper mass ratio, the optimal damping ratio is decreasing when mass tuning ratio increases.

The variations of the dynamic responses of the primary structures controlled by H_2 optimized NSIA-TMD ($\mu = 0.50$) versus frequency ratio for different values of damping ratios have been displayed in Fig. 6. Eqs. (28), (B.1), (29), and (B.2) are implemented to obtain optimal frequency and damping ratios for Fig. 6. The system parameters are considered as $\mu_d = 0.03$, $\mu_T = 0.01$, $\mu = 0.50$, and $\theta = 14^\circ$. P, Q, R, and S are the fixed points in Fig. 6.

As a result, the optimal values for the NSIA-TMD's frequency and damping ratios are obtained as 0.8583 and 0.17, respectively. At $\zeta_b = 0$, it was noticed that the primary structure's displacement response was unconstrained. As a result, the displacement amplitudes are unrestrained at their respective Eigen frequencies (i.e., $\eta = 0.7769, 1.112, 1.987, 1.992$). When

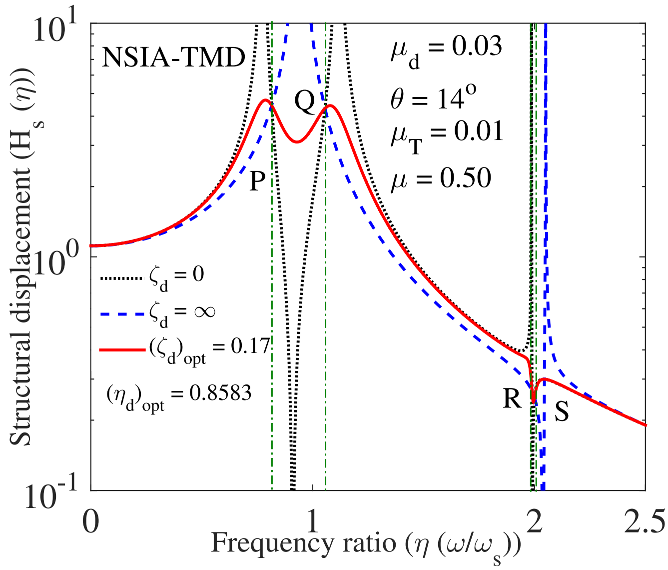

Fig. 6. The variations of the dynamic responses of the primary structures controlled by H_2 optimized NSIA-TMD ($\mu = 0.50$) versus frequency ratio for the different values of damping ratios.

the damping ratio of the NSIA-TMD is increased, the responses across the domain of system resonances are attenuated. This displacement graph may also be used to find the resonance, minimum areas [16]. At $\eta = 0.7885, 1.079$, the resonance peaks have been discovered. Due to NSIA-TMD damping, there has been a movement away from the eigen frequencies. The minima frequency region's peak has likewise been determined to be $\eta = 0.9294$. The anti-resonance frequency region's peak has been detected at $\eta = 1.995$. The log plots were used to detect the resonant, anti-resonance, minimum frequency peaks in these displacement graphs. The primary structure's maximum displacement response has been calculated to be 4.6878. When the NSIA-TMD damping goes to ∞, the controlled structure's displacement peaks merge into one. As a result, the displacement peaks of the primary structure and the tuned mass damper have been connected. Double peaks are shown, signifying that the whole system has been compressed to a 2DOF system.

The variations of the dynamic responses of the primary structures controlled by H_2 optimized NS-TMD ($\mu = 0$) versus frequency ratio for different values of damping ratios have been displayed in Fig. 7(a). Eqs. (28), (B.1), (29), and (B.2) are implemented to obtain optimal frequency and damping ratios for Fig. 7(a).

The system parameters are considered as $\mu_d = 0.03$, $\mu_T = 0.01$, $\mu = 0$, and $\theta = 14^\circ$. P, Q, R, and S are the fixed points in Fig. 7(a).

As a result, the optimal values for the NS-TMD's frequency and damping ratios are obtained as 0.8469 and 0.17, respectively. At $\zeta_b = 0$, it was noticed that the primary structure's displacement response was unconstrained. As a result, the displacement amplitudes are unrestrained at their respective eigen frequencies (i.e., $\eta = 0.7626, 1.118, 1.974, 1.980$). When the damping ratio of the NS-TMD is increased, the responses across the domain of system resonances are attenuated. This displacement graph may also be used to find the resonance, minimum areas [16]. At $\eta = 0.7771, 1.082$, the resonance peaks have been discovered. Due to NS-TMD damping, there has been a movement away from the eigen frequencies. The minima frequency region's peak has likewise been determined to be $\eta = 0.9252$. The anti-resonance frequency region's peak has been detected at $\eta = 1.99$. The log plots were used to detect the resonant, anti-resonance, minimum frequency peaks in these displacement graphs. The primary structure's maximum displacement response has been calculated to be 4.5069. When the NS-TMD damping goes to ∞, the controlled structure's displacement peaks merge into one. As a result, the displacement peaks of the primary structure and the tuned mass damper have been connected. Double peaks are shown, signifying that the whole system has been compressed to a 2DOF system.

The variations of the dynamic responses of the primary structures controlled by H_2 optimized IA-TMD ($\mu = 1.0$) versus frequency ratio for different values of damping ratios have been displayed in Fig. 7(b). Eqs. (28), (B.1), (29), and (B.2) are implemented to obtain optimal frequency and damping ratios for Fig. 7(b). The system parameters are considered as $\mu_d = 0.03$, $\mu_T = 0.01$, $\mu = 1$, and $\theta = 14^\circ$. P and Q indicate two fixed points in Fig. 7(b).

As a result, the optimal values for the IA-TMD's frequency and damping ratios ratios are obtained as 0.8703 and 0.16. At $\zeta_b = 0$, it was noticed that the primary structure's displacement response was unconstrained. As a result, the displacement amplitudes are unbounded at their respective Eigen frequencies (i.e., $\eta = 0.7972, 1.076$). When the damping ratio of the IA-TMD is increased, the responses across the domain of system resonances are attenuated. This displacement graph may also be used to find the resonance, minimum areas [16]. At $\eta = 0.786, 1.107$, the resonance peaks have been discovered. Due to IA-TMD damping, there has been a movement away from the eigen frequencies. The minima frequency region's peak

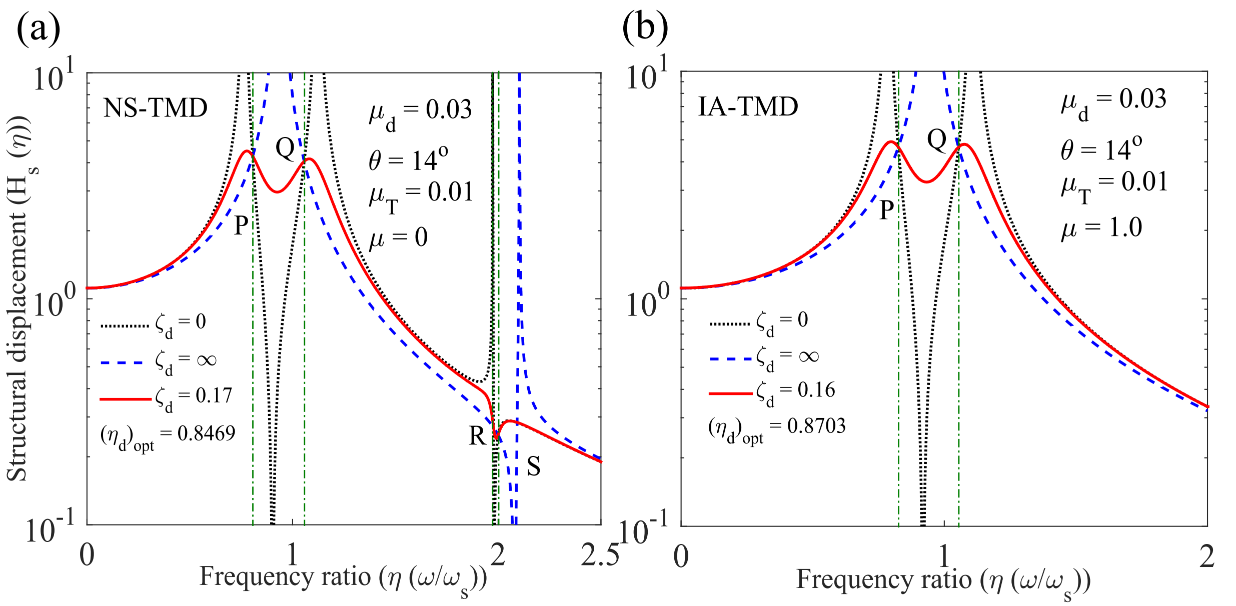

Fig. 7. The variations of the dynamic responses of the primary structures controlled by H_2 optimized NS-TMD ($\mu = 0$) versus frequency ratio for the different values of damping ratios. (b) The variations of the dynamic responses of the primary structures controlled by H_2 optimized IA-TMD ($\mu = 1.0$) versus frequency ratio for the different values of damping ratios.

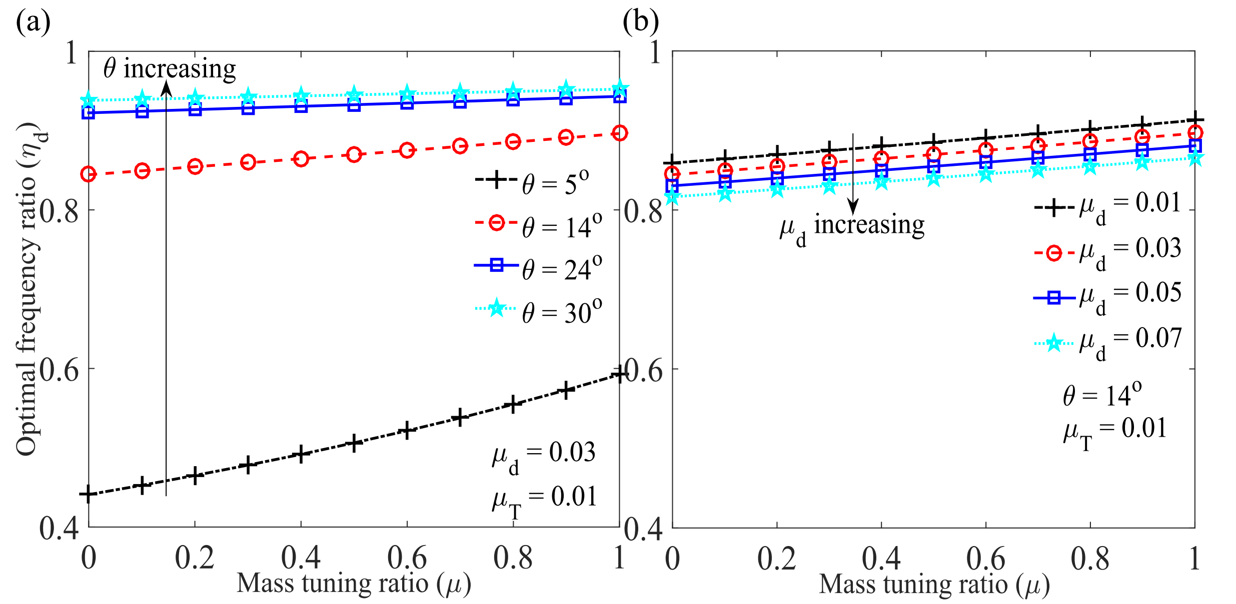

Fig. 8. The variations of optimal frequency ratio η_d versus mass tuning ratio μ for different values of (a) inertial angle θ and (b) damper mass ratio μ_d of novel tuned mass dampers.

has likewise been determined to be $\eta = 0.9332$. The log plots were used to detect the resonant, anti-resonance, minimum frequency peaks in these displacement graphs. The primary structure's maximum displacement response has been calculated to be 4.9029. When the IA-TMD damping goes to ∞, the controlled structure's displacement peaks merge into one. As a result, the displacement peaks of the primary structure and the tuned mass damper have been connected. Single peak is shown, signifying that the whole system has been compressed to an SDOF system.

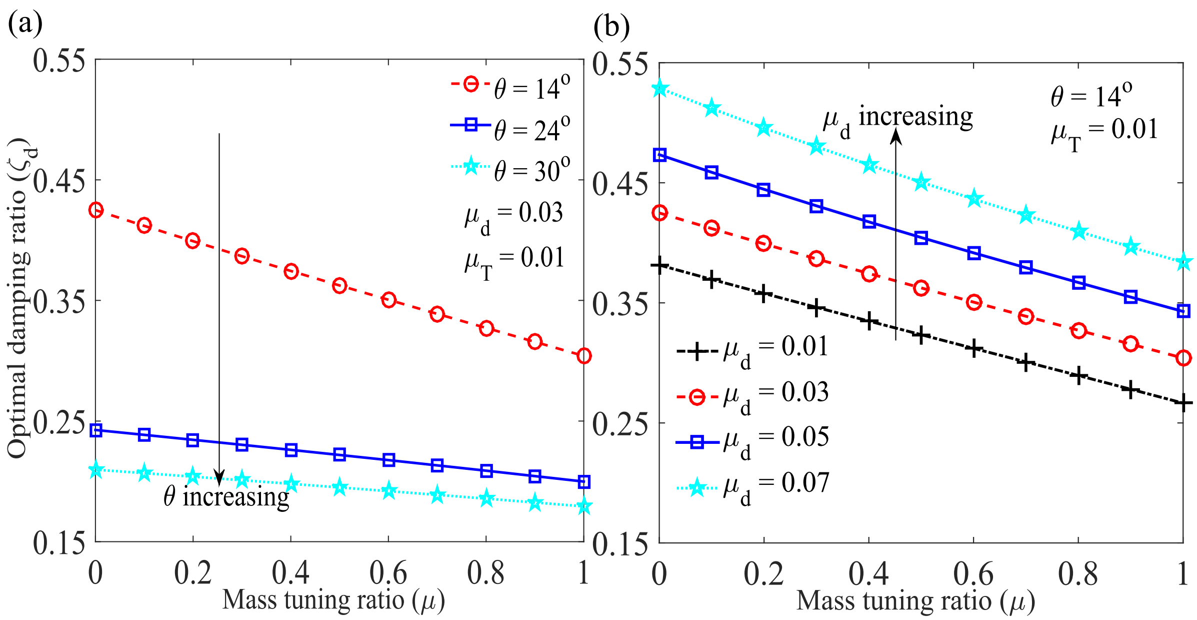

Fig. 9. The variations of optimal viscous damping ratio ζ_d versus mass tuning ratio μ for different values of (a) inertial angle θ and (b) damper mass ratio μ_d of novel tuned mass dampers.

3.3. H_∞ optimization

The variations of η_d versus μ for different values of θ are displayed in Fig. 8(a). The black ($\theta = 5^\circ$), red ($\theta = 14^\circ$), blue ($\theta = 24^\circ$), and cyan ($\theta = 30^\circ$) lines with markers are applied to identify each plot. The system parameters are considered as $\mu_T = 0.01$ and $\mu_d = 0.03$.

The optimal frequency ratio of novel tuned mass dampers increases as the inertial angle of the amplifier increases. Thus, the natural frequency of novel tuned mass dampers increases, as do the restoring forces, possibly reducing primary dynamic system deflections during vibration. The inverse effect occurs as the damper mass ratio increases.

The variations of optimal frequency ratio η_d versus mass tuning ratio μ of the novel tuned mass dampers for the different values of damper mass ratio μ_d have been displayed in Fig. 8(b). The black ($\mu_d = 0.01$), red ($\mu_d = 0.03$), blue ($\mu_d = 0.05$), and cyan ($\mu_d = 0.07$) lines with markers are applied to identify each plot. The system parameters are considered as $\mu_T = 0.01$ and $\theta = 14^\circ$. The optimal frequency ratio increases as the mass tuning ratio of the novel tuned mass dampers increase and decreases as the damper mass ratio increases. Therefore, the natural frequency of novel tuned mass dampers decreases, whereas the structure's time period increases, potentially reducing primary dynamic system deflections during vibration. However, for both Fig. 8(a) and (b), the optimal frequency ratio is increasing when the mass tuning ratio increases. Thus, the natural frequency of novel tuned mass dampers increases, as do the restoring forces, possibly reducing primary dynamic system deflections during vibration.

The variations of optimal damping ratio ζ_d versus mass tuning ratio μ of the novel tuned mass dampers for the different values of inertial angle θ have been displayed in Fig. 9(a). The red ($\theta = 14^\circ$), blue ($\theta = 24^\circ$), and cyan ($\theta = 30^\circ$) lines with markers are applied to identify each plot. The system parameters are considered as $\mu_T = 0.01$ and $\mu_d = 0.03$. The optimal damping ratio of novel tuned mass dampers decreases as the inertial angle of the amplifier increases. Thus, the damping increases at a lower damping ratio for IA-TMD and slightly higher for NS-TMD and NSIA-TMD, as does the damping force reduction capacity, possibly reducing the primary dynamic system's deflections during vibration effectively. In contrast, the damping ratio increases as the damper mass ratio increases, which has been observed from Fig. 9(b). The black ($\mu_d = 0.01$), red ($\mu_d = 0.03$), blue ($\mu_d = 0.05$), and cyan ($\mu_d = 0.07$) lines with markers are applied to identify each plot. The system parameters are considered as $\mu_T = 0.10$ and $\theta = 14^\circ$. As the damper mass ratio increases, the optimal damping ratio also increases. Thus, a higher damper mass ratio provides additional damping force reduction capacity, enabling these dampers to surpass conventional tuned mass dampers in terms of response reduction capacity.

The variations of the dynamic responses of the primary structures controlled by H_∞ optimized NSIA-TMD ($\mu = 0.50$) versus frequency ratio for different values of damping ratios have been displayed in Fig. 10. Eqs. (43), (45), and (46) are implemented to obtain optimal frequency and damping ratios for Fig. 10. The system parameters are considered as $\mu_d = 0.03$, $\mu_T = 0.01$, $\mu = 0.50$, and $\theta = 14^\circ$. For all graphs, P, Q, and R are indicating three fixed points. P, Q, R are the fixed points in Fig. 10.

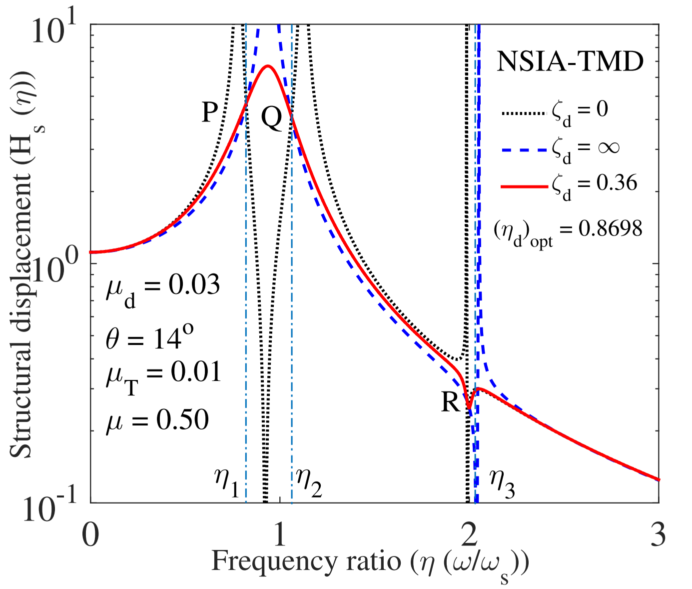

Fig. 10. The variations of the dynamic responses of the primary structures controlled by H_∞ optimized NSIA-TMD ($\mu = 0.50$) versus frequency ratio for the different values of damping ratios.

As a result, the optimal values for the NSIA-TMD's frequency and damping ratios are obtained as 0.8698 and 0.36, respectively. At $\zeta_b = 0$, it was noticed that the primary structure's displacement response was unconstrained. As a result, the displacement amplitudes are unbounded at their respective eigen frequencies (i.e., $\eta = 0.7773, 1.117, 1.986$). When the damping ratio of the NSIA-TMD is increased, the responses across the domain of system resonances are attenuated. This displacement graph may also be used to find the resonance, minimum areas [16]. At $\eta = 0.9353$, the resonance peak has been discovered. Due to NSIA-TMD damping, there has been a movement away from the eigen frequencies. The anti-resonance frequency region's peak has been detected at $\eta = 1.999$. The log plots were used to detect the resonant, anti-resonance, minimum frequency peaks in these displacement graphs. The primary structure's maximum displacement response has been calculated to be 6.6852. When the NSIA-TMD damping goes to ∞, the controlled structure's displacement peaks merge into one. As a result, the displacement peaks of the primary structure and the tuned mass damper have been connected. Double peaks are shown, signifying that the whole system has been compressed to a 2DOF system.

The variations of the dynamic responses of the primary structures controlled by H_∞ optimized NS-TMD ($\mu = 0$) versus frequency ratio for different values of damping ratios have been displayed in Fig. 11(a). Eqs. (43), (45), and (46) are implemented to obtain optimal frequency and damping ratios for Fig. 11(a). The system parameters are considered as $\mu_d = 0.03$, $\mu_T = 0.01$, $\mu = 0$, and $\theta = 14^\circ$. P, Q, R are the fixed points in Fig. 11(a).

As a result, the optimal values for the NS-TMD's frequency and damping ratios are obtained as 0.8446 and 0.42, respectively. At $\zeta_b = 0$, it was noticed that the primary structure's displacement response was unconstrained. As a result, the displacement amplitudes are unbounded at their respective eigen frequencies (i.e., $\eta = 0.7651, 1.122, 1.974$). When the damping ratio of the NS-TMD is increased, the responses across the domain of system resonances are attenuated. This displacement graph may also be used to find the resonance, minimum areas [16]. At $\eta = 0.9353$, the resonance peak has been discovered. Due to NS-TMD damping, there has been a movement away from the eigen frequencies. The anti-resonance frequency region's peak has been detected at $\eta = 2.001$. The log plots were used to detect the resonant, anti-resonance, minimum frequency peaks in these displacement graphs. The primary structure's maximum displacement response has been calculated to be 7.1530. When the NS-TMD damping goes to ∞, the controlled structure's displacement peaks merge into one. As a result, the displacement peaks of the primary structure and the tuned mass damper have been connected. Double peaks are shown, signifying that the whole system has been compressed to a 2DOF system.

The variations of the dynamic responses of the primary structures controlled by H_∞ optimized IA-TMD ($\mu = 1.0$) versus frequency ratio for different values of damping ratios have been displayed in Fig. 11(b). Eqs. (43), (45), and (46) are implemented to obtain optimal frequency and damping ratios for Fig. 11(b). The system parameters are considered as $\mu_d = 0.03$, $\mu_T = 0.01$, $\mu = 1.0$, and $\theta = 14^\circ$. P, Q are the fixed points in Fig. 11(b).

As a result, the optimal values for the IA-TMD's frequency and damping ratios are obtained as 0.8965 and 0.30, respectively. At $\zeta_b = 0$, it was noticed that the primary structure's displacement response was unconstrained. As a result, the displacement amplitudes are unbounded at their respective eigen frequencies (i.e., $\eta = 0.8008, 1.12$). When the damping ratio of the IA-TMD is increased, the responses across the domain of system resonances are attenuated. This displacement graph may also be used to find the resonance, minimum areas [16]. At $\eta = 0.9189$, the resonance peaks have been dis-

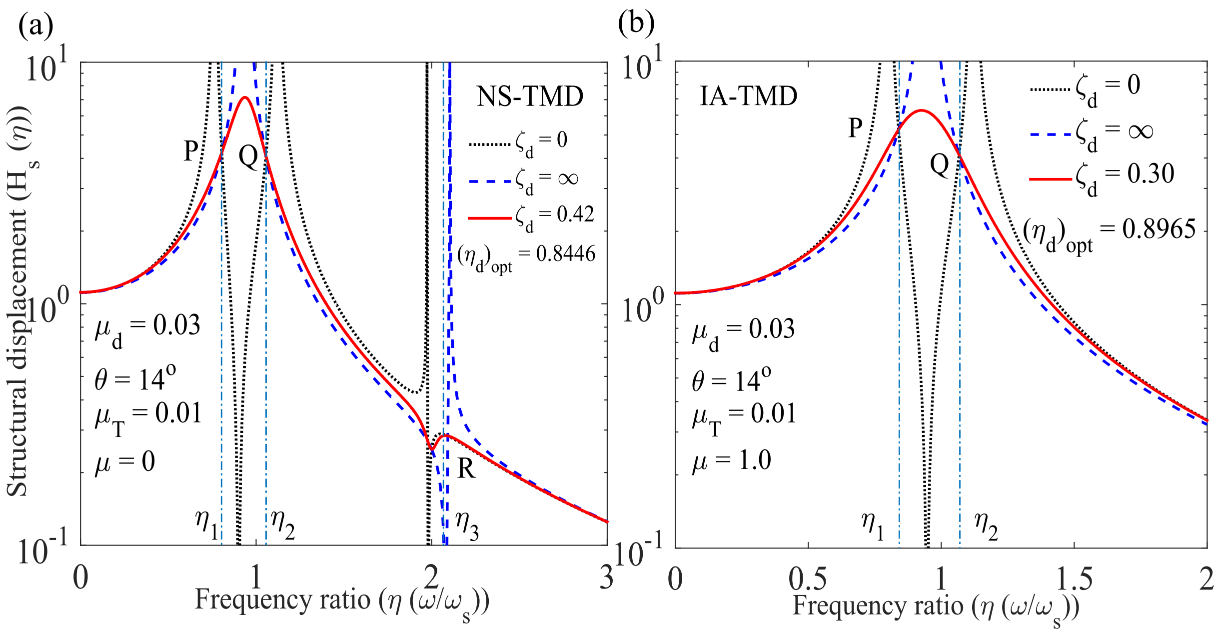

Fig. 11. The variations of the dynamic responses of the primary structures controlled by H_∞ optimized NS-TMD ($\mu = 0$) versus frequency ratio for the different values of damping ratios. (b) The variations of the dynamic responses of the primary structures controlled by H_∞ optimized IA-TMD ($\mu = 1.0$) versus frequency ratio for the different values of damping ratios.

Table 2
H_2 optimized design parameters in terms of closed-form expressions for novel tuned mass dampers and traditional tuned mass dampers.

System	Proposed by	H_2 optimization	
		η_d	ζ_d
NS-TMD	This study	Eq. (B.1)	Eq. (B.2)
NSIA-TMD	This study	Eq. (B.1)	Eq. (B.2)
IA-TMD	This study	Eq. (B.1)	Eq. (B.2)
TMD	Iwata [97], Warburton et al. [98]	$\frac{1}{1+\gamma}\sqrt{\frac{2+\gamma}{2}}$	$\sqrt{\frac{\gamma(4+3\gamma)}{8(1+\gamma)(2+\gamma)}}$
TMD	Warburton et al. [98], Zilletti [99]	$\frac{1}{\sqrt{1+\gamma}}$	$\frac{\sqrt{\gamma}}{2}$

Where $\gamma = \mu_d + 2(\mu_a + \mu_b)$; total static mass of novel tuned mass dampers and traditional tuned mass dampers are equal.

covered. Due to IA-TMD damping, there has been a movement away from the eigen frequencies. The primary structure's maximum displacement response has been calculated to be 6.2731. When the IA-TMD damping goes to ∞, the controlled structure's displacement peaks merge into one. As a result, the displacement peaks of the primary structure and the tuned mass damper have been connected. Single peak is shown, signifying that the whole system has been compressed to an SDOF system.

3.4. Performance evaluation of optimized novel tuned mass dampers in comparison to optimized traditional tuned mass dampers

The variations of structural displacement versus frequency ratio for uncontrolled structure and structure controlled by H_2 optimized novel tuned mass dampers, traditional tuned mass damper (TMD) are shown in Fig. 12. For Fig. 12(a), Eqs. (B.1) and (B.2) are implemented to obtain optimal frequency and damping ratio for H_2 optimized novel tuned mass dampers. For traditional tuned mass damper, the closed-form equations for optimal design parameters are adopted from Iwata [97], Warburton et al. [98]. The exact closed-form expressions for H_2 optimized design parameters of novel tuned mass dampers and traditional tuned mass dampers are listed in Table 2. The damping ratio for structure has been considered as 0.01 (i.e., $\zeta_s = 0.01$). The peak displacement of uncontrolled structure determines as 50.0025. The peak displacement of structure controlled by traditional TMD determines as 7.5055. The peak displacement of structure controlled by NS-TMD determines as 4.3684. The peak displacement of structure controlled by IA-TMD determines as 4.7237. The peak displacements of structure controlled by NSIA-TMD determine as 4.3991, 4.4308, 4.4634, 4.4970, 4.5317, 4.5676, 4.6047, 4.6430, 4.6826.

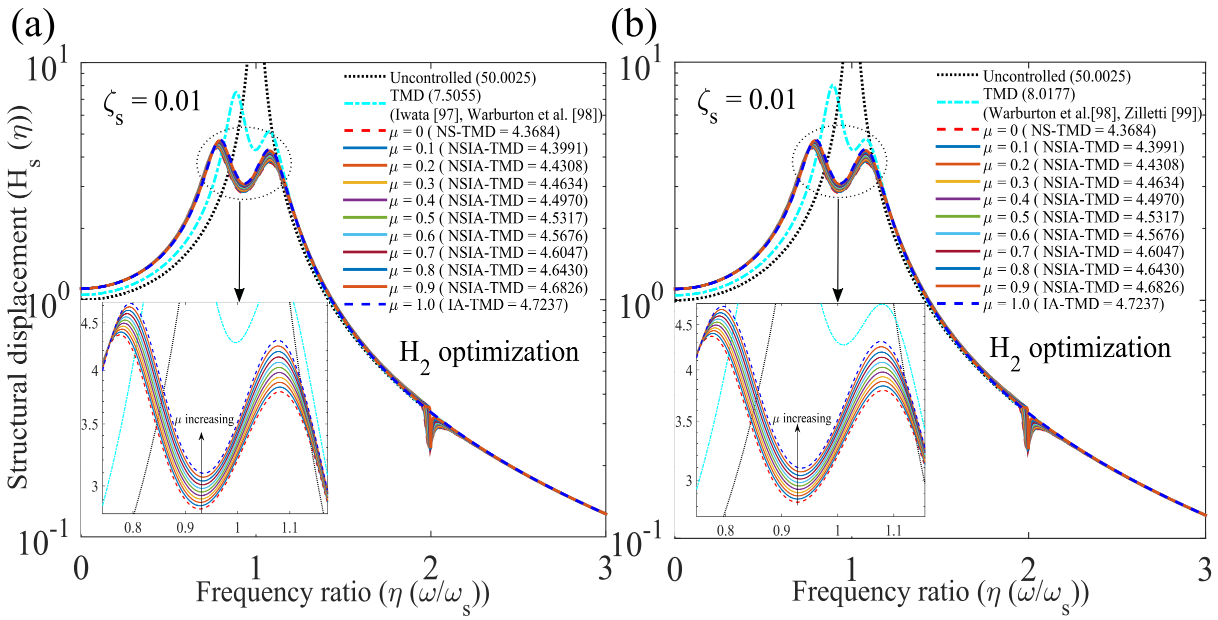

Fig. 12. (a) The variations of structural displacement $H_s(\eta)$ versus frequency ratio η for uncontrolled structure and structure controlled by H_2 optimized novel tuned mass dampers, traditional tuned mass damper (TMD-Iwata [97], Warburton et al. [98]). (b) The variations of structural displacement $H_s(\eta)$ versus frequency ratio η for uncontrolled structure and structure controlled by H_2 optimized novel tuned mass dampers, traditional tuned mass damper (TMD- Warburton et al. [98], Zilletti [99]). Eqs. (B.1) and (B.2) are implemented to obtain the optimal frequency and damping ratio for H_2 optimized novel tuned mass dampers.

Based on the derived results, the response reduction capacities of H_2 optimized NS-TMD, NSIA-TMD, and IA-TMD have been determined in comparison to the H_2 optimized traditional TMD. Therefore, the response reduction capacities of H_2 optimized NS-TMD, NSIA-TMD, and IA-TMD 41.79%, 39.62%, 37.06% superior to the H_2 optimized traditional TMD proposed by Iwata [97], Warburton et al. [98].

Fig. 12 (b) shows the variations of structural displacement $H_s(\eta)$ versus frequency ratio η for uncontrolled structure and structure controlled by H_2 optimized novel tuned mass dampers, traditional tuned mass damper. For this figure, the optimal closed-form expression for traditional tuned mass dampers have been adopted from Warburton et al. [98], Zilletti [99]. Eqs. (B.1) and (B.2) are implemented to determine optimal frequency and damping ratio for H_2 optimized novel tuned mass dampers. The peak dynamic response of the primary structure controlled by traditional TMD is obtained as 8.0177. The peak dynamic response of the primary structure controlled by NS-TMD determines as 4.3684. The peak dynamic response of the primary structure controlled by IA-TMD determines as 4.7237. The peak dynamic responses of the primary structures controlled by NSIA-TMD systems are determined as 4.3991, 4.4308, 4.4634, 4.4970, 4.5317, 4.5676, 4.6047, 4.6430, 4.6826. Therefore, the dynamic response reduction capacities of H_2 optimized NS-TMD, NSIA-TMD, and IA-TMD 45.51%, 43.47%, 41.08% superior to the H_2 optimized traditional TMD proposed by Warburton et al. [98], Zilletti [99]. Overall, the dynamic response reduction capacity of H_2 optimized NS-TMD is significantly superior to the H_2 optimized NSIA-TMD and H_2 optimized IA-TMD, depicting that the performance of novel tuned mass dampers decreases as the mass tuning ratio increases.

The variations of dynamic responses of the primary structures controlled by novel tuned mass dampers vs frequency ratio have been displayed in Fig. 13. The primary structure's damping ratio considers as 0.01 (i.e., $\zeta_s = 0.01$). Eq. (B.1) and Eq. (B.2) are implemented to determine the frequency and viscous damping ratios for novel tuned mass dampers.

For all three figures (i.e., Fig. 13(a)–(c)), the displacement responses of primary structures are increasing when the values of inertial angle increase. Overall results show that the dynamic response reduction capacity of novel tuned mass dampers are downgraded when the inertial angle increases. Therefore, to acquire the optimum vibration reduction capacity from novel tuned mass dampers, lower inertial angle θ has been recommended, respectively.

The variations of dynamic responses of the primary structures versus frequency ratio for the uncontrolled structure and structures controlled by H_∞ optimized novel tuned mass dampers, traditional tuned mass damper (TMD) are shown in Fig. 14.

For Fig. 14(a), Eqs. (43), (45), and (46) are implemented to obtain optimal frequency and damping ratios for H_∞ optimized novel tuned mass dampers. For traditional tuned mass damper, the closed-form equations for optimal design parameters has been adopted from Ormondroyd and Den Hartog [2], Nishihara and Asami [100]. The exact closed-form expressions for H_∞ optimized design parameters of novel tuned mass dampers and traditional tuned mass dampers are listed in Table 3. The damping ratio for structure has been considered as 0.01 (i.e., $\zeta_s = 0.01$). The maximum displacement of uncontrolled structure determines as 50.0025. The peak displacement of structure controlled by traditional TMD determines as 6.6325. The

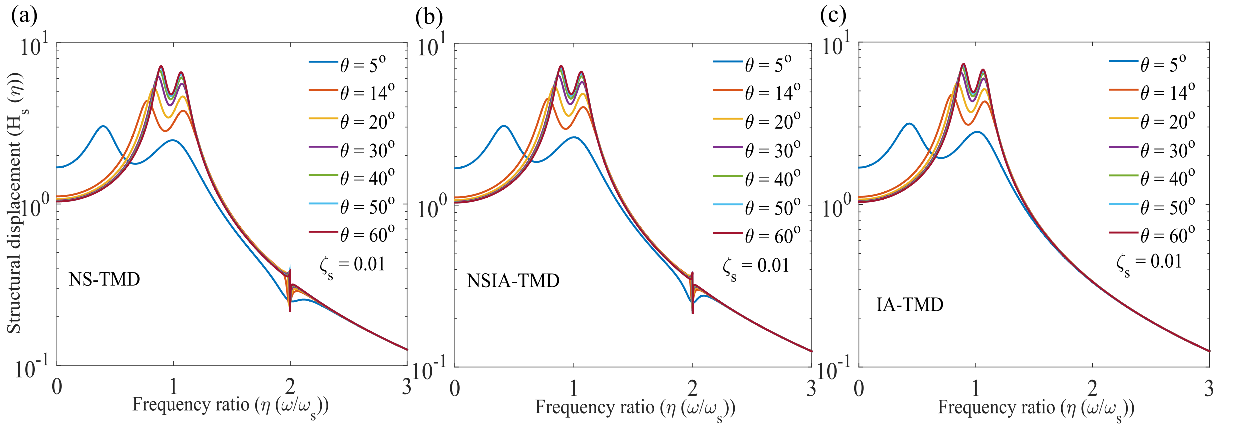

Fig. 13. The variations of structural displacement $H_s(\eta)$ versus frequency ratio η for structures controlled by (a) NS-TMD, (b) NSIA-TMD, and (c) IA-TMD for different values of θ.

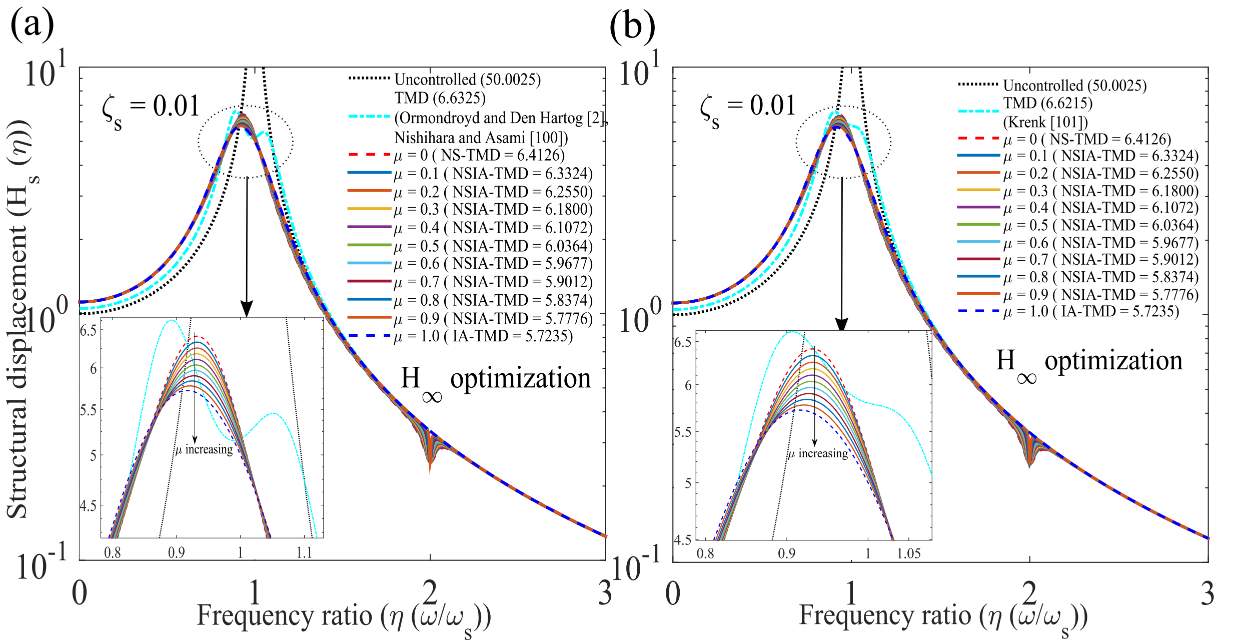

Fig. 14. (a) The variations of structural displacement $H_s(\eta)$ versus frequency ratio η for uncontrolled structure and structure controlled by H_∞ optimized novel tuned mass dampers, traditional tuned mass damper (TMD-Ormondroyd and Den Hartog [2], Nishihara and Asami [100]). (b) The variations of structural displacement $H_s(\eta)$ versus frequency ratio η for uncontrolled structure and structure controlled by H_∞ optimized novel tuned mass dampers, traditional tuned mass damper (TMD- Krenk [101]). Eqs. (43), (45), and (46) are implemented to obtain optimal frequency and damping ratios for H_∞ optimized novel tuned mass dampers.

Table 3
The values of H_∞ optimized design parameters for novel tuned mass dampers and traditional tuned mass dampers.

System	Proposed by	H_∞ optimization	
		η_d	ζ_d
NS-TMD	This study	Eq. (43)	Eq. (46)
NSIA-TMD	This study	Eq. (43)	Eq. (46)
IA-TMD	This study	Eq. (43)	Eq. (46)
TMD	Ormondroyd and Den Hartog [2] Nishihara and Asami [100]	$\frac{1}{1+\gamma}$	$\sqrt{\frac{3\gamma}{8(1+\gamma)}}$
TMD	Krenk [101]	$\frac{1}{1+\gamma}$	$\sqrt{\frac{\gamma}{2(1+\gamma)}}$

Where $\gamma = \mu_d + 2(\mu_a + \mu_b)$; total static mass of novel tuned mass dampers and traditional tuned mass dampers are equal.

peak displacement of structure controlled by NS-TMD determines as 6.4126. The peak displacement of structure controlled by IA-TMD determines as 5.7235. The peak displacements of structure controlled by NSIA-TMD determine as 6.3324, 6.2550, 6.1800, 6.1072, 6.0364, 5.9677, 5.9012, 5.8374, 5.7776.

Based on the derived results, the response reduction capacities of H_∞ optimized NS-TMD, NSIA-TMD, and IA-TMD have been determined in comparison to the H_∞ optimized traditional TMD. Therefore, the response reduction capacities of H_∞ optimized NS-TMD, NSIA-TMD, and IA-TMD 3.31%, 8.98%, 13.79% superior to the traditional TMD. Fig. 14(b) shows the variations of structural displacement $H_s(\eta)$ versus frequency ratio η for uncontrolled structure and structure controlled by H_∞ optimized novel tuned mass dampers, traditional tuned mass damper. For this figure, the optimal closed-form expression for traditional tuned mass dampers have been adopted from Krenk [101]. Eqs. (43), (45), and (46) are implemented to obtain optimal frequency and damping ratios for H_∞ optimized novel tuned mass dampers.

The peak dynamic response of the primary structure controlled by traditional TMD has been determined as 6.6215. The peak dynamic response of the primary structure controlled by NS-TMD determines as 6.4216. The peak dynamic response of the primary structure controlled by IA-TMD determines as 5.7235. The peak dynamic responses of the primary structures controlled by NSIA-TMD systems are determined as 6.3324, 6.2550, 6.1800, 6.1072, 6.0364, 5.9677, 5.9012, 5.8374, 5.7776. Therefore, the dynamic response reduction capacities of H_∞ optimized NS-TMD, NSIA-TMD, and IA-TMD 3.01%, 8.83%, 13.56% superior to the traditional TMD.

Overall, the dynamic response reduction capacity of H_∞ optimized IA-TMD is significantly superior to the H_∞ optimized NS-TMD and H_∞ optimized NSIA-TMD, depicting that the performance of novel tuned mass dampers increases as the mass tuning ratio increases.

4. Nonlinear dynamic analysis of nonlinear negative stiffness inertial amplifier tuned mass dampers

Now, large-amplitude vibrations are addressed for tuned mass dampers with negative stiffness inertial amplifiers. In the process of large-amplitude vibrations, these novel dampers have caused substantial deflections, enabling the nonlinear kinematics mechanism to be applied in these passive vibration control systems. The effective mass for the vertical spring mass systems are derived as

$$m_e = (1-\mu)m_T\left(\tfrac{k_b}{k_b-m_b\omega^2}\right) + \mu m_T = (1-\mu)m_T\left(\tfrac{1}{1-\frac{\omega^2}{\omega_b^2}}\right) + \mu m_T \tag{47}$$

After considering large-amplitude deflections in x and y-directions, the closed-form expressions for displacements of effective mass m_e in x and y-directions have been derived as

$$x_a = \frac{u_s+u_d}{2} \quad \text{and} \quad y_a = l\sin\theta - \sqrt{l^2\sin^2\theta - x_d l\cos\theta - \frac{x_d^2}{4}} \tag{48}$$

where $x_d = u_d - u_s$, defines the relative displacement of novel dampers w.r.t the main structure. Eq. (48) has been differentiated with respect to time 't'. Therefore, the exact closed-form expressions for velocity responses are derived as

$$\dot{x}_a = \frac{\dot{u}_s+\dot{u}_d}{2} \quad \text{and} \quad \dot{y}_a = \frac{(2l\cos\theta + x_d)\dot{x}_d}{\sqrt{16l^2\sin^2\theta - 16x_d l\cos\theta - 4x_d^2}} \tag{49}$$

where $(\bullet)$ refers the derivative with respect to time. Applying Eq. (49), the total kinetic energies for novel dampers are derived as

$$\begin{aligned} E_k &= \tfrac{1}{2}m_d\dot{u}_d^2 + 2\times\tfrac{1}{2}m_e\left(\dot{x}_a^2+\dot{y}_a^2\right) \\ &= \tfrac{1}{2}m_d\dot{u}_d^2 + \tfrac{m_e\dot{x}_d^2(2l\cos\theta+x_d)^2}{16l^2\sin^2\theta-16x_d l\cos\theta-4x_d^2} + \tfrac{m_e(\dot{u}_s+\dot{u}_d)^2}{4} \end{aligned} \tag{50}$$

The total potential energy for these novel dampers are derived as

$$E_v = \tfrac{1}{2}k_d x_d^2 \tag{51}$$

Therefore, the Lagrange's equations [102] are applied to derive the equations of motion for the novel dampers. The Lagrange's equations are listed below.

$$\tfrac{d}{dt}\left(\tfrac{\partial E_k}{\partial \dot{x}_j}\right) - \tfrac{\partial E_k}{\partial x_j} + \tfrac{\partial E_v}{\partial x_j} + \tfrac{\partial E_d}{\partial \dot{x}_j} = 0 \tag{52}$$

where E_d is the energy dissipated by the novel dampers.x_j defines the coordinates of $x_d = u_d - u_s$ and $x_s = u_s - x_g$, j refers to the subscript for nominating the main structure and damper. The relative displacement of the main structure with respect to the ground is defined by x_s. Therefore, the equation of motion for dampers has been derived as

$$\underbrace{\left(m_d + \frac{2m_e l^2}{4l^2\sin^2\theta - 4x_d l\cos\theta - x_d^2}\right)}_{m_{ad}}\ddot{x}_d + k_d x_d = -(m_e+m_d)\ddot{x}_g \tag{53}$$

Therefore, the total effective mass for the novel dampers are derived as

$$m_{ad} = \left(m_d + \frac{2m_e l^2}{4l^2 \sin^2\theta - 4x_d l \cos\theta - x_d^2} \right) \tag{54}$$

However, to produce nonlinear dynamic responses of the controlled structure analytically, m_{ad} needs to be generalized using Taylor expansions at the static equilibrium [59] (i.e., $x_d = 0$). Therefore, the generalized effective mass for novel dampers has been derived as

$$\begin{aligned} m_{ad} &= m_0 + m_1 x_d + m_2 x_d^2 \\ &= \underbrace{m_d + 0.5 m_e \left(1 + \frac{1}{\tan^2\theta}\right)}_{m_0} + \underbrace{\frac{\cos\theta\, m_e}{2l\sin^4\theta}}_{m_1} x_d + \underbrace{\frac{(1+3\cos^2\theta) m_e}{4l^2 \sin^6\theta}}_{m_2} x_d^2 \end{aligned} \tag{55}$$

The equations of motion of the dynamic systems controlled by novel tuned mass dampers have already been derived as

$$\begin{aligned} & m_{ad}\ddot{x}_d + c_{ad}\dot{x}_d + k_{ad}x_d + m_{ad}\ddot{x}_s = -m_{ad}\ddot{x}_g \\ & m_s\ddot{x}_s + c_s\dot{x}_s + k_s x_s - c_{ad}\dot{x}_d - k_{ad}x_d = -m_s\ddot{x}_g \end{aligned} \tag{56}$$

The nonlinear equations of motion for the controlled structures have been produced after substituting Eq. (55) into Eq. (56). Therefore, the nonlinear equations of motion of structure controlled by nonlinear novel tuned mass dampers have been derived as

$$\begin{aligned} & m_0\ddot{x}_d + 2m_0\,\zeta_d\,\omega_d\,\dot{x}_d + m_0\,\omega_d{}^2 x_d + m_1\,x_d\ddot{x}_d + 2\,m_1\,\zeta_d\,\omega_d\,x_d\dot{x}_d + m_1\,\omega_d{}^2\,x_d^2 \\ & + m_2\,x_d{}^2\ddot{x}_d + 2\,m_2\,\zeta_d\,\omega_d x_d{}^2\dot{x}_d + m_2\,\omega_d{}^2 x_d{}^3 + m_0\ddot{x}_s + m_1\,x_d\ddot{x}_s + m_2\,x_d{}^2\ddot{x}_s \\ & = -m_0\ddot{x}_g - m_1\,x_d\ddot{x}_g - m_2\,x_d{}^2\ddot{x}_g \\ & m_s\ddot{x}_s + c_s\dot{x}_s + k_s x_s - 2m_0\,\zeta_d\,\omega_d\,\dot{x}_d - 2\,m_1\,\zeta_d\,\omega_d\,x_d\dot{x}_d - 2\,m_2\,\zeta_d\,\omega_d x_d{}^2\dot{x}_d \\ & - m_0\,\omega_d{}^2 x_d - m_1\,\omega_d{}^2\,x_d^2 - m_2\,\omega_d{}^2 x_d{}^3 = -m_s\ddot{x}_g \end{aligned} \tag{57}$$

The above equations seem to be very nonlinear. Initially, equivalent linearization method has been applied to determine the dynamic responses of structures controlled by nonlinear novel tuned mass dampers. Each nonlinear element of the equations of motion have been linearized individually [95]. To perform this linearization process, zero mean has been considered. Therefore, the linearized form of each nonlinear element has been derived as

$$\begin{aligned} & m_{d1}^e = E\left\{\frac{\partial(m_1\,x_d\ddot{x}_d)}{\partial\ddot{x}_d}\right\} = 0 && \text{and} \quad m_{d2}^e = E\left\{\frac{\partial(m_2\,x_d{}^2\ddot{x}_d)}{\partial\ddot{x}_d}\right\} = 0 \\ & c_{d1}^e = E\left\{\frac{\partial(2\,m_1\,\zeta_d\,\omega_d\,x_d\dot{x}_d)}{\partial\dot{x}_d}\right\} = 0 && \text{and} \quad c_{d2}^e = E\left\{\frac{\partial(2\,m_2\,\zeta_d\,\omega_d x_d{}^2\dot{x}_d)}{\partial\dot{x}_d}\right\} = 0 \\ & k_{d1}^e = E\left\{\frac{\partial(m_1\,\omega_d{}^2\,x_d^2)}{\partial x_d}\right\} = 0 && \text{and} \quad k_{d2}^e = E\left\{\frac{\partial(m_2\,\omega_d{}^2 x_d{}^3)}{\partial x_d}\right\} = 3m_2\omega_d^2\sigma_{x_d}^2 \\ & m_{s1}^e = E\left\{\frac{\partial(m_1\,x_d\ddot{x}_s)}{\partial\ddot{x}_s}\right\} = 0 && \text{and} \quad m_{s2}^e = E\left\{\frac{\partial(m_2\,x_d{}^2\ddot{x}_s)}{\partial\ddot{x}_s}\right\} = 0 \\ & m_{g1}^e = E\left\{\frac{\partial(m_1\,x_d\ddot{x}_g)}{\partial\ddot{x}_g}\right\} = 0 && \text{and} \quad m_{g2}^e = E\left\{\frac{\partial(m_2\,x_d{}^2\ddot{x}_g)}{\partial\ddot{x}_g}\right\} = 0 \end{aligned} \tag{58}$$

Eq. (58) has been substituted in Eq. (57), which leads to

$$\begin{aligned} & m_0\ddot{x}_d + 2m_0\,\zeta_d\,\omega_d\,\dot{x}_d + m_0\,\omega_d{}^2 x_d + 3m_2\omega_d^2\sigma_{x_d}^2 x_d + m_0\ddot{x}_s && = -m_0\ddot{x}_g \\ & m_s\ddot{x}_s + c_s\dot{x}_s + k_s x_s - 2m_0\,\zeta_d\,\omega_d\,\dot{x}_d - m_0\,\omega_d{}^2 x_d - 3m_2\omega_d^2\sigma_{x_d}^2 x_d && = -m_s\ddot{x}_g \end{aligned} \tag{59}$$

The steady state solutions are derived as $x_d = X_d e^{i\omega t}$, $x_s = X_s e^{i\omega t}$, and $\ddot{X}_g = A_g e^{i\omega t}$ for harmonic base excitation. The steady state solutions are substituted in Eq. (59) to derive the transfer function for evaluating the dynamic responses of the controlled structures. Hence, the transfer function has been derived as

$$\begin{bmatrix} \left(3\,\sigma_{x_d}{}^2\mu_2 + \mu_0\right)\omega_d{}^2 + 2\,q\zeta_d\,\omega_d\mu_0 + q^2\mu_0 & q^2\mu_0 \\ -3\,\sigma_{x_d}{}^2\mu_2\omega_d{}^2 - 2\,q\zeta_d\,\omega_d\mu_0 - \mu_0\omega_d{}^2 & 2\,\zeta_s\,\omega_s\,q + q^2 + \omega_s{}^2 \end{bmatrix} \begin{Bmatrix} X_d \\ X_s \end{Bmatrix} = -\begin{bmatrix} \mu_0 \\ 1 \end{bmatrix} A_g \tag{60}$$

where $q = i\omega$, $\mu_0 = (\tilde{\mu}_1\,\omega_b{}^2 + q^2\tilde{\mu}_2)/(q^2 + \omega_b{}^2)$, $\tilde{\mu}_1 = \tilde{m}_1/m_s = (\Theta\,\mu_T + \mu_d)$, $\tilde{\mu}_2 = \tilde{m}_2/m_s = (\Theta\,\mu_T\mu + \mu_d)$, and $\Theta = 0.5\left(1 + \frac{1}{\tan^2\theta}\right)$. μ_0 defines the mass ratio of 1st effective mass m_0 of novel nonlinear tuned mass dampers to the primary structure m_s, μ_T refers the ratio of the total static mass at one side vertical terminal to the mass of the primary structure m_s, μ_d denotes the ratio of static mass of novel dampers to the primary structure m_s. $k_{3d} = 3\,\mu_2\omega_d{}^2\sigma_{x_d}{}^2 + \omega_d{}^2\mu_0$, defines the effective stiffness of equivalent linearized nonlinear tuned mass dampers. Therefore, the exact closed-form expression for the dynamic responses of the nonlinear tuned mass dampers has been derived as

$$H_d(q) = \frac{X_d}{A_g} = \frac{-(2\,q\zeta_s + \omega_s)\mu_0\omega_s}{\Delta} \tag{61}$$

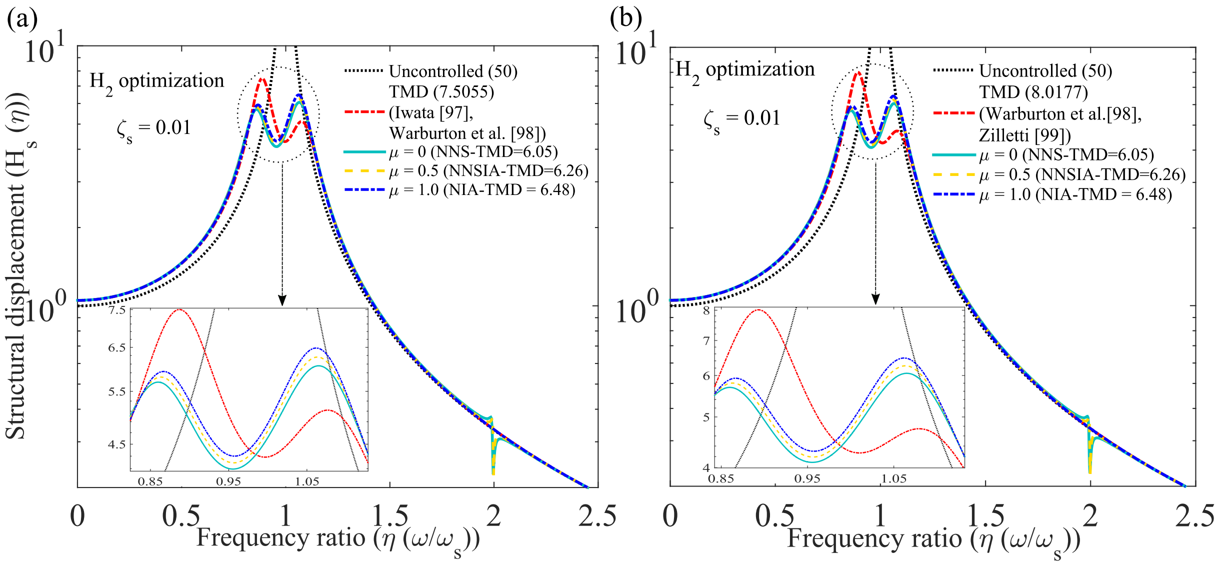

Fig. 15. The variations of dynamic responses of the uncontrolled structure and structures controlled by H_2 optimized TMD, NNS-TMD, NNSIA-TMD, and NIA-TMD. For TMD, the optimal design parameters are adopted from the published papers, studied by Iwata [97], Warburton et al. [98], and Zilletti [99].

The exact closed-form expression for dynamic responses of the primary structures are derived as

$$H_s(q) = \frac{X_d}{A_g} = \frac{\begin{array}{c} -3\,\sigma_{x_d}{}^2\mu_0\mu_2\omega_d{}^2 - 2\,q\zeta_d\,\omega_d\mu_0{}^2 - 3\,\sigma_{x_d}{}^2\mu_2\omega_d{}^2 \\ -2\,q\zeta_d\,\omega_d\mu_0 - \mu_0{}^2\omega_d{}^2 - q^2\mu_0 - \mu_0\omega_d{}^2 \end{array}}{\Delta} \tag{62}$$

The closed-form expressions for Δ has been derived as

$$\Delta = \begin{array}{c} q^4\mu_0 + \left(2\,\zeta_d\,\mu_0{}^2\omega_d + 2\,\zeta_d\,\mu_0\omega_d + 2\,\zeta_s\,\omega_s\,\mu_0\right)q^3 \\ +\left(\begin{array}{c} 3\,\sigma_{x_d}{}^2\mu_0\mu_2\omega_d{}^2 + 4\,\zeta_d\,\zeta_s\,\mu_0\omega_s\,\omega_d + 3\,\sigma_{x_d}{}^2\mu_2\omega_d{}^2 \\ +\mu_0{}^2\omega_d{}^2 + \omega_s{}^2\mu_0 + \mu_0\omega_d{}^2 \end{array}\right)q^2 \\ +\left(6\,\zeta_s\,\omega_s\,\sigma_{x_d}{}^2\mu_2\omega_d{}^2 + 2\,\zeta_d\,\omega_s{}^2\mu_0\omega_d + 2\,\zeta_s\,\omega_s\,\mu_0\omega_d{}^2\right)q \\ +3\,\omega_s{}^2\sigma_{x_d}{}^2\mu_2\omega_d{}^2 + \omega_s{}^2\mu_0\omega_d{}^2 \end{array} \tag{63}$$

To derive the closed-form expression for $\sigma_{x_d}{}^2$ from Eq. (60), initially, considers $\sigma_{x_d}{}^2 = 0$. Now, it has been considered that the controlled structures are subjected to white-noise random base excitation. The viscous damping ratio of the primary structures are considered as zero (i.e., $\zeta_s = 0$. Hence, Eq. (61) has been modified as

$$H_d(q) = \frac{X_d}{A_g} = \frac{-\left(q^2+\omega_b{}^2\right)\omega_s{}^2}{\begin{array}{c} q^6 + \left(2\,\tilde{\mu}_2\,\zeta_d\,\omega_d + 2\,\zeta_d\,\omega_d\right)q^5 \\ +\left(\omega_d{}^2\mu_2 + \omega_b{}^2 + \omega_s{}^2 + \omega_d{}^2\right)q^4 \\ +\left(2\,\tilde{\mu}_1\,\zeta_d\,\omega_b{}^2\omega_d + 2\,\zeta_d\,\omega_b{}^2\omega_d + 2\,\zeta_d\,\omega_s{}^2\omega_d\right)q^3 \\ +\left(\tilde{\mu}_1\,\omega_b{}^2\omega_d{}^2 + \omega_b{}^2\omega_s{}^2 + \omega_b{}^2\omega_d{}^2 + \omega_s{}^2\omega_d{}^2\right)q^2 \\ +2\,q\zeta_d\,\omega_b{}^2\omega_s{}^2\omega_d + \omega_b{}^2\omega_s{}^2\omega_d{}^2 \end{array}} \tag{64}$$

Therefore, using Eq. (64), the standard deviation for dynamic response [16,94] of nonlinear novel tuned mass damper $\sigma_{x_d}{}^2$ has been derived as

$$\sigma_{x_d}^2 = \frac{S_0\pi\left(\begin{array}{c} -\tilde{\mu}_1^2\omega_b{}^4\omega_d{}^2 + \tilde{\mu}_1\,\tilde{\mu}_2\,\omega_b{}^2\omega_s{}^2\omega_d{}^2 - \tilde{\mu}_1\,\omega_b{}^4\omega_s{}^2 \\ -2\,\tilde{\mu}_1\,\omega_b{}^4\omega_d{}^2 - \tilde{\mu}_1\,\omega_b{}^2\omega_s{}^2\omega_d{}^2 + \tilde{\mu}_2\,\omega_b{}^2\omega_s{}^4 \\ +2\,\tilde{\mu}_2\,\omega_b{}^2\omega_s{}^2\omega_d{}^2 + \tilde{\mu}_2\,\omega_s{}^4\omega_d{}^2 - \omega_b{}^4\omega_d{}^2 \end{array}\right)}{2\,\omega_b{}^4\zeta_d\left(\tilde{\mu}_1\,\omega_b{}^2 - \tilde{\mu}_2\,\omega_s{}^2\right)\omega_s{}^4\omega_d{}^3} \tag{65}$$

The variations of optimal displacement responses of primary structure controlled by H_2 optimized tuned mass damper (TMD), nonlinear negative stiffness tuned mass damper (NNS-TMD), nonlinear negative stiffness inertial amplifier tuned mass damper (NNSIA-TMD), and nonlinear inertial amplifier tuned mass damper (NIA-TMD) have been shown in Fig. 15. The variations of the dynamic responses of the uncontrolled structure have also been varied to investigate the optimum dynamic response reduction capacity of proposed nonlinear tuned mass dampers. The viscous damping ratio of the primary structures considers as $\zeta_s = 0.01$. The system parameters for nonlinear mass dampers are considered as $\mu_d = 0.03$, $\mu_T = 0.01$, $\eta_b = 2.0$, and $\theta = 30^\circ$. $\mu = 0$, $\mu = 0.5$, and $\mu = 1.0$ are considered for NNS-TMD, NNSIA-TMD, and NIA-TMD. The length

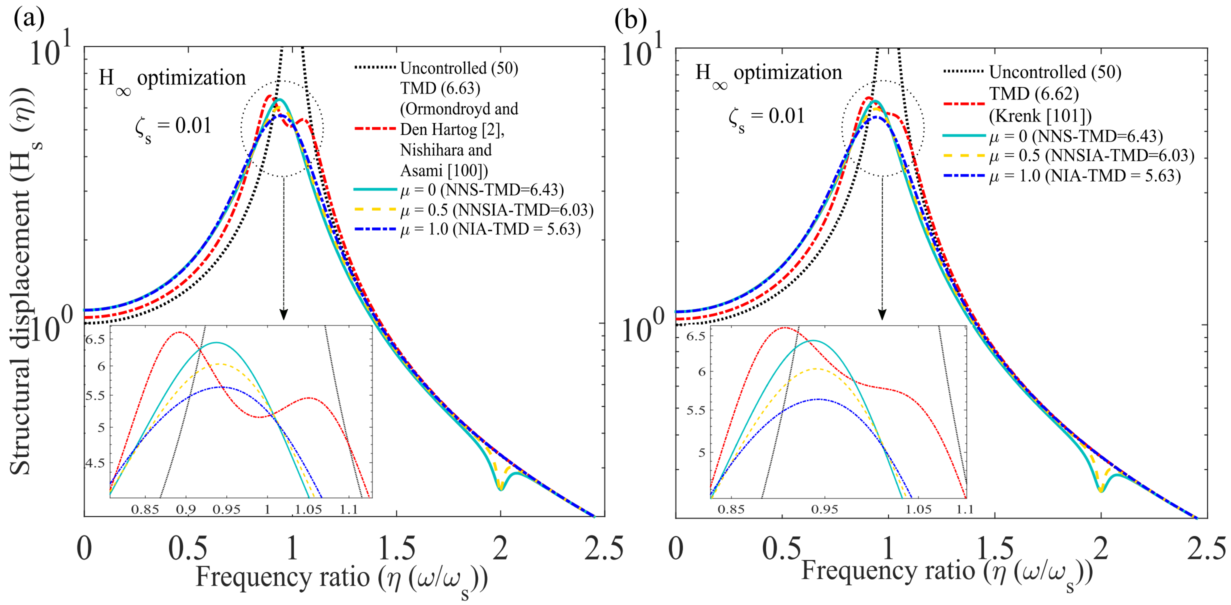

Fig. 16. The variations of dynamic responses of the uncontrolled structure and structures controlled by H_∞ optimized TMD, NNS-TMD, NNSIA-TMD, and NIA-TMD. For TMD, the optimal design parameters are adopted from the published papers, studied by Ormondroyd and Den Hartog [2], Nishihara and Asami [100], and Krenk [101].

of the rigid links has been considered as $l = 0.05$ m. The time period of the main structure is considered as $T_s = 0.5$ s. $S_0 = 1N^2$ s kg^{-2} has been considered as the constant spectral density for white-noise random excitation. Eqs. (B.1) and (B.2) have been applied to determine optimal frequency and damping ratio for H_2 optimized novel tuned mass dampers. The maximum displacement of the uncontrolled structure has been determined as 50. The maximum displacement of primary structure controlled by TMD, studied by Iwata [97], Warburton et al. [98] has been determined as 7.5055. The maximum displacements of primary structure controlled by nonlinear negative stiffness tuned mass damper (NNS-TMD), nonlinear negative stiffness inertial amplifier tuned mass damper (NNSIA-TMD), and nonlinear inertial amplifier tuned mass damper (NIA-TMD) have been derived as 6.05, 6.26, and 6.48. Therefore, the dynamic response reduction capacities of NNS-TMD, NNSIA-TMD, and NIA-TMD have been determined as 87.90%, 87.48%, and 87.04%. The dynamic response reduction capacities of these novel nonlinear dampers are also been compared with the traditional tuned mass dampers, studied by Iwata [97], Warburton et al. [98].

Therefore, the dynamic response reduction capacities of NNS-TMD, NNSIA-TMD, and NIA-TMD are significantly 19.39%, 16.59%, and 13.66% superior to the TMD, studied by Iwata [97], Warburton et al. [98]. The variations of the dynamic response of primary structures controlled by TMD, studied by Warburton et al. [98], and Zilletti [99] have been shown in Fig. 15(b). The dynamic response reduction capacities of NNS-TMD, NNSIA-TMD, and NIA-TMD are compared with the TMD, studied by Warburton et al. [98], and Zilletti [99]. The peak displacement of the primary structure controlled by TMD has been determined as 8.0177. Therefore, the dynamic response reduction capacities of NNS-TMD, NNSIA-TMD, and NIA-TMD are significantly 24.54%, 21.92%, and 19.12% superior to the TMD, studied by Warburton et al. [98], and Zilletti [99]. The variations of optimal dynamic responses of the primary structures controlled by H_∞ optimized tuned mass damper (TMD), nonlinear negative stiffness tuned mass damper (NNS-TMD), nonlinear negative stiffness inertial amplifier tuned mass damper (NNSIA-TMD), and nonlinear inertial amplifier tuned mass damper (NIA-TMD) have been shown in Fig. 16. The variations of displacements of the uncontrolled structure have also been varied to investigate the optimum vibration reduction capacity of proposed nonlinear tuned mass dampers. The viscous damping ratio of the main structure has been considered as $\zeta_s = 0.01$. The system parameters for nonlinear mass dampers are considered as $\mu_d = 0.03$, $\mu_T = 0.01$, $\eta_b = 2.0$, and $\theta = 14^\circ$. $\mu = 0$, $\mu = 0.5$, and $\mu = 1.0$ are considered for NNS-TMD, NNSIA-TMD, and NIA-TMD. The length of the rigid links has been considered as $l = 0.10$ m. The time period of the main structure is considered as $T_s = 0.5$ s. $S_0 = 1N^2$ s kg^{-2} has been considered as the constant spectral density for white-noise random excitation. Eqs. (43), (45) and (46) are applied to determine optimal frequency and damping ratio for H_∞ optimized novel tuned mass dampers.

The peak dynamic response of the uncontrolled structure has been determined as 50. The peak dynamic response of primary structure controlled by TMD, studied by Ormondroyd and Den Hartog [2], Nishihara and Asami [100] has been determined as 6.63. The peak dynamic responses of primary structure controlled by nonlinear negative stiffness tuned mass damper (NNS-TMD), nonlinear negative stiffness inertial amplifier tuned mass damper (NNSIA-TMD), and nonlinear inertial amplifier tuned mass damper (NIA-TMD) have been derived as 6.43, 6.03, and 5.63. Therefore, the dynamic response reduction capacities of NNS-TMD, NNSIA-TMD, and NIA-TMD have been determined as 87.14%, 87.94%, and 88.74%. The dynamic response reduction capacities of these novel nonlinear dampers are also been compared with the traditional tuned mass dampers, studied by Ormondroyd and Den Hartog [2], Nishihara and Asami [100]. Therefore, the dynamic response reduction capacities of NNS-TMD, NNSIA-TMD, and NIA-TMD are significantly 3.01%, 9.04%, and 15.08% superior to the TMD, studied by Ormondroyd and Den Hartog [2], Nishihara and Asami [100]. The variations of the dynamic responses of the primary structure controlled by TMD, studied by Krenk [101] and proposed nonlinear tuned mass dampers are shown in Fig. 16(b). Hence, the maximum dynamic response of the TMD, studied by Krenk [101] has also been determined as 6.62. Therefore, the dynamic response reduction capacities of NNS-TMD, NNSIA-TMD, and NIA-TMD are significantly 2.87%, 8.89%, and 14.95% superior to the TMD, studied by Krenk [101].

5. Summary and conclusions

The negative stiffness tuned mass dampers (NS-TMD), negative stiffness inertial amplifier tuned mass dampers (NSIA-TMD), and inertial amplifier tuned mass dampers (IA-TMD) are introduced in this paper. Two distinct novel tuned mass dampers are derived from NSIA-TMD: negative stiffness tuned mass damper (NS-TMD) and inertial amplifier tuned mass damper (IA-TMD), are mathematically developed by altering the mass tuning ratio of NSIA-TMD, keeping the combined static mass of the entire system constant. The negative stiffness inertial amplifier tuned mass dampers (NSIA-TMD) are increased the system's dynamic mass significantly and provided dynamic negative stiffness. As a result, it increases the dynamic response reduction capacity of the traditional tuned mass damper (TMD), keeping the total static mass constant. The exact closed-form expressions for optimal design parameters of these novel tuned mass dampers subjected to random-white noise and harmonic excitations were driven by the H_2 and H_∞ optimization methods. The nonlinear negative stiffness inertial amplifier tuned mass damper (NNSIA-TMD), nonlinear negative stiffness tuned mass damper (NNS-TMD), and nonlinear inertial amplifier tuned mass damper (NIA-TMD) for single degree of freedom systems (SDOF) are also introduced in this paper. Finally, the dynamic response reduction capacities of H_2 and H_∞ optimized novel tuned mass dampers were compared to the dynamic response reduction capacities of H_2 and H_∞ optimized traditional tuned mass dampers. The significant outcomes are listed below.

- For both H_2 and H_∞ optimization techniques, the optimal frequency ratio of novel dampers are increasing when mass tuning ratio increases.
- For both H_2 and H_∞ optimization techniques, the optimal damping ratio of novel dampers are decreasing when mass tuning ratio increases.
- The lower value of inertial angle has been recommended to design optimal novel tuned mass dampers to acquire maximum vibration reduction capacity.
- The dynamic response reduction capacity of H_2 optimized NS-TMD is significantly superior to the H_2 optimized NSIA-TMD and H_2 optimized IA-TMD, depicting that the performance of novel tuned mass dampers decreases as the mass tuning ratio increases. Besides, the dynamic response reduction capacity of H_∞ optimized IA-TMD is significantly superior to the H_∞ optimized NS-TMD and H_∞ optimized NSIA-TMD, depicting that the performance of novel tuned mass dampers increases as the mass tuning ratio increases.
- The dynamic response reduction capacities of H_2 optimized NS-TMD, NSIA-TMD, and IA-TMD are significantly 41.79%, 39.62%, 37.06% superior to the H_2 optimized traditional TMD proposed by Iwata [97], Warburton et al. [98]. Furthermore, the dynamic response reduction capacities of H_2 optimized NS-TMD, NSIA-TMD, and IA-TMD are significantly 41.79%, 39.62%, 37.06% superior to the H_2 optimized traditional TMD proposed by Iwata [97], Warburton et al. [98].
- The dynamic response reduction capacities of H_∞ optimized NS-TMD, NSIA-TMD, and IA-TMD are significantly 3.31%, 8.98%, 13.79% superior to the H_∞ optimized traditional TMD proposed by Ormondroyd and Den Hartog [2], Nishihara and Asami [100]. Furthermore, the dynamic response reduction capacities of H_∞ optimized NS-TMD, NSIA-TMD, and IA-TMD are significantly 3.01%, 8.83%, 13.56% superior to the traditional TMD proposed by Krenk [101].
- The dynamic response reduction capacities of H_2 optimized NNS-TMD, NNSIA-TMD, and NIA-TMD are significantly 19.39%, 16.59%, 13.66% superior to the H_2 optimized traditional TMD proposed by Iwata [97], Warburton et al. [98]. Furthermore, the dynamic response reduction capacities of H_2 optimized NS-TMD, NSIA-TMD, and IA-TMD are significantly 24.54%, 21.92%, 19.12% superior to the H_2 optimized traditional TMD proposed by Iwata [97], Warburton et al. [98].
- The dynamic response reduction capacities of H_∞ optimized NNS-TMD, NNSIA-TMD, and NIA-TMD are significantly 3.01%, 9.04%, 15.08% superior to the H_∞ optimized traditional TMD proposed by Ormondroyd and Den Hartog [2], Nishihara and Asami [100]. Furthermore, the dynamic response reduction capacities of H_∞ optimized NNS-TMD, NNSIA-TMD, and NIA-TMD are significantly 2.87%, 8.89%, 14.95% superior to the traditional TMD proposed by Krenk [101].

The paper's novelty lies in proposing novel negative stiffness inertial amplifier tuned mass dampers, which are not present in the state of the art based on the author's best knowledge. The paper makes several significant contributions. Additionally, the proposition of the new closed-form expressions for optimal design parameters of the novel tuned mass dampers is another significant contribution of this paper. These equations resulted in the optimal design of these novel tuned mass dampers, resulting in the maximum amount of vibration reduction. The practical realization, experimentation, and prototyping of the proposed negative stiffness inertial amplifier tuned mass dampers will be the future scope of the research.

Declaration of Competing Interest

The authors declare that they have no known competing financial interests or personal relationships that could have appeared to influence the work reported in this paper

Acknowledgments

The authors' would like to acknowledge the Inspire faculty grant, grant number DST/ INSPIRE/04/2018/000052 for partial financial support for the project. SC would like to acknowledge the MHRD grant received from IIT Delhi during the period of this research work.

Appendix A. Closed-form equations from (Section 2.2)

The dynamic responses of the novel tuned mass dampers have been derived as

$$H_d(q) = \frac{X_d}{A_g} = \frac{-(2\,q\zeta_s + \omega_s)\omega_s\left(q^2 + {\omega_b}^2\right)}{\Delta_n} \tag{A.1}$$

The shear force of the entire controlled systems have been derived as

$$\begin{aligned} H_{sf}(q) &= \frac{q\zeta_s X_s + \omega_s^2 X_s}{A_g} \\ &= \frac{\begin{pmatrix} -q^4 + (-2\,\mu_2\,\zeta_d\,\omega_d - 2\,\zeta_d\,\omega_d)q^3 + \left(-{\omega_d}^2\mu_2 - {\omega_b}^2 - {\omega_d}^2\right)q^2 \\ +\left(-2\,\mu_1\,\zeta_d\,{\omega_b}^2\omega_d - 2\,\zeta_d\,{\omega_b}^2\omega_d\right)q - {\omega_b}^2{\omega_d}^2\mu_1 - {\omega_b}^2{\omega_d}^2 \end{pmatrix}\left(q\zeta_s + {\omega_s}^2\right)}{\Delta_n} \end{aligned} \tag{A.2}$$

Appendix B. Closed-form equations from H_2 optimization (Section 2.5)

The non-dimensional form of Eq. (28) has been listed below.

$$(\eta_d)_{opt} = \sqrt{\frac{3\,\mu_1\,{\eta_b}^6 + 2\,{\eta_b}^6 - {\mu_1}^3{\eta_b}^6 + {\mu_1}^2\mu_2\,{\eta_b}^4 - 3\,\mu_2\,{\eta_b}^4 - 2\,{\eta_b}^4}{\begin{matrix} 2\,{\mu_1}^4{\eta_b}^6 - 2\,{\mu_1}^3\mu_2\,{\eta_b}^4 + 8\,{\mu_1}^3{\eta_b}^6 + 4\,{\mu_1}^3{\eta_b}^4 + 12\,{\mu_1}^2{\eta_b}^6 \\ +8\,\mu_1\,{\eta_b}^6 - 12\,{\mu_1}^2\mu_2\,{\eta_b}^4 - 4\,{\mu_1}^2\mu_2\,{\eta_b}^2 + 4\,\mu_1\,{\mu_2}^2{\eta_b}^2 \\ +6\,{\mu_1}^2{\eta_b}^4 + 2\,{\mu_1}^2{\eta_b}^2 - 18\,\mu_1\,\mu_2\,{\eta_b}^4 - 8\,\mu_1\,\mu_2\,{\eta_b}^2 \\ +6\,{\mu_2}^2{\eta_b}^2 + 2\,{\mu_2}^2 - 8\,\mu_2\,{\eta_b}^4 + 2\,{\eta_b}^6 - 2\,{\eta_b}^4 - 2\,\mu_1\,\mu_2 \end{matrix}}} \tag{B.1}$$

where $\eta_d = \omega_d/\omega_s$, defines the optimal frequency ratio of damper to main dynamic system.

The non-dimensional form of Eq. (29) has been listed below.

$$(\zeta_d)_{opt} = \sqrt{\frac{\left(\mu_1\,{\eta_b}^2 - \mu_2\right)\begin{pmatrix} 20\,{\mu_1}^2{\eta_b}^6 - {\mu_1}^5{\eta_b}^6 + {\mu_1}^4\mu_2\,{\eta_b}^4 + 10\,{\mu_1}^3{\eta_b}^6 \\ +15\,\mu_1\,{\eta_b}^6 - 4\,{\mu_1}^3{\eta_b}^4 - 6\,{\mu_1}^2\mu_2\,{\eta_b}^4 - 12\,{\mu_1}^2{\eta_b}^4 \\ -8\,{\mu_1}^2{\eta_b}^2 - 8\,\mu_1\,\mu_2\,{\eta_b}^4 + 4\,{\eta_b}^6 + 8\,\mu_1\,\mu_2\,{\eta_b}^2 \\ -12\,\mu_1\,{\eta_b}^4 - 8\,\mu_1\,{\eta_b}^2 - 4\,\mu_1 - 3\,\mu_2\,{\eta_b}^4 + 4\,\mu_2 \\ -4\,{\eta_b}^4 + 8\,\mu_2\,{\eta_b}^2 \end{pmatrix}}{\begin{matrix} 8\,{\eta_b}^2\left(3\,\mu_1\,{\eta_b}^2 + 2\,{\eta_b}^2 - {\mu_1}^3{\eta_b}^2 + {\mu_1}^2\mu_2 - 3\,\mu_2 - 2\right) \\ \begin{pmatrix} \mu_1^3{\eta_b}^4 - {\mu_1}^2\mu_2\,{\eta_b}^2 + 3\,{\mu_1}^2{\eta_b}^4 + {\mu_1}^2{\eta_b}^2 - 4\,\mu_1\,\mu_2\,{\eta_b}^2 \\ -\mu_2\mu_1 + {\mu_2}^2 + 3\,\mu_1\,{\eta_b}^4 - 3\,\mu_2\,{\eta_b}^2 + {\eta_b}^4 - {\eta_b}^2 \end{pmatrix} \end{matrix}}} \tag{B.2}$$

Appendix C. Closed-form equations from H_∞ optimization (Section 2.6)

The displacement response of the novel tuned mass dampers is derived as

$$H_d(\eta) = \frac{X_d}{A_g}\omega_s^2 = \frac{\eta^2 - {\eta_b}^2 + 2\,\zeta_s\,i\eta\left(\eta^2 - {\eta_b}^2\right)}{\Delta_n} \tag{C.1}$$

References

[1] H. Frahm, Devices for damping vibration of bodies, US Patent (989958) (1909).
[2] J. Ormondroyd, The theory of the dynamic vibration absorber, Trans., ASME, Appl. Mech. 50 (1928) 9–22.
[3] M.Z. Chen, Y. Hu, Analysis for inerter-based vibration system, in: Inerter and Its Application in Vibration Control Systems, Springer, 2019, pp. 19–39.
[4] H. Sun, L. Zuo, X. Wang, J. Peng, W. Wang, Exact H_2 optimal solutions to inerter-based isolation systems for building structures, Struct. Control Health Monit. 26 (6) (2019) e2357.
[5] D. Čakmak, Z. Tomičević, H. Wolf, Ž. Božić, D. Semenski, Stability and performance of supercritical inerter-based active vibration isolation systems, J. Sound Vib. 518 (2021) 116234.

[6] M. Baduidana, A. Kenfack-Jiotsa, Optimal design of inerter-based isolators minimizing the compliance and mobility transfer function versus harmonic and random ground acceleration excitation, J. Vib. Control 27 (11–12) (2021) 1297–1310.
[7] J.P. Den Hartog, Mechanical Vibrations, Courier Corporation, 1985.
[8] S. Kopylov, Z. Chen, M.A. Abdelkareem, Implementation of an electromagnetic regenerative tuned mass damper in a vehicle suspension system, IEEE Access 8 (2020) 110153–110163.
[9] S. Adhikari, S. Bhattacharya, Dynamic analysis of wind turbine towers on flexible foundations, Shock Vib. 19 (1) (2012) 37–56.
[10] J. Wang, C. Lin, B. Chen, Vibration suppression for high-speed railway bridges using tuned mass dampers, Int. J. Solids Struct. 40 (2) (2003) 465–491.
[11] A. Batou, S. Adhikari, Optimal parameters of viscoelastic tuned-mass dampers, J. Sound Vib. 445 (2019) 17–28.
[12] G. Barone, M. Di Paola, F.L. Iacono, G. Navarra, Viscoelastic bearings with fractional constitutive law for fractional tuned mass dampers, J. Sound Vib. 344 (2015) 18–27.
[13] G. Pipitone, G. Barone, A. Palmeri, Stochastic design of double-skin façades as seismic vibration absorbers, Adv. Eng. Softw. 142 (2020) 102749.
[14] S. Kasinos, A. Palmeri, M. Lombardo, S. Adhikari, A reduced modal subspace approach for damped stochastic dynamic systems, Comput. Struct. 257 (2021) 106651.
[15] M. De Angelis, F. Petrini, D. Pietrosanti, Optimal design of the ideal grounded tuned mass damper inerter for comfort performances improvement in footbridges with practical implementation considerations, Struct. Control Health Monit. 28 (9) (2021) e2800.
[16] S. Chowdhury, A. Banerjee, S. Adhikari, Optimal negative stiffness inertial-amplifier-base-isolators: exact closed-form expressions, Int. J. Mech. Sci. 218 (2022) 107044.
[17] S.R. Patro, A. Banerjee, S. Adhikari, G. Ramana, Kaimal spectrum based H2 optimization of tuned mass dampers for wind turbines, J. Vib. Control (2022). SAGE Publications Sage UK, London, England, 10775463221092838
[18] A. Sinha, Optimal damped vibration absorber for narrow band random excitations: a mixed H_2/H_∞ optimization, Probab. Eng. Mech. 24 (2) (2009) 251–254.
[19] T. Asami, O. Nishihara, A.M. Baz, Analytical solutions to H_∞ and H_2 optimization of dynamic vibration absorbers attached to damped linear systems, J. Vib. Acoust. 124 (2) (2002) 284–295.
[20] T. Asami, O. Nishihara, H_2 optimization of the three-element type dynamic vibration absorbers, J. Vib. Acoust. 124 (4) (2002) 583–592.
[21] Y. Cheung, W.O. Wong, H_2 optimization of a non-traditional dynamic vibration absorber for vibration control of structures under random force excitation, J. Sound Vib. 330 (6) (2011) 1039–1044.
[22] A. Palmeri, M. Lombardo, A new modal correction method for linear structures subjected to deterministic and random loadings, Comput. Struct. 89 (11–12) (2011) 844–854.
[23] H.H. Khodaparast, J.E. Mottershead, M.I. Friswell, Perturbation methods for the estimation of parameter variability in stochastic model updating, Mech. Syst. Signal Process. 22 (8) (2008) 1751–1773.
[24] H.H. Khodaparast, J. Mottershead, Efficient methods in stochastic model updating, Stoch. Model. 7 (8) (2008) 9.
[25] S. Adhikari, M. Friswell, G. Litak, H.H. Khodaparast, Design and analysis of vibration energy harvesters based on peak response statistics, Smart Mater. Struct. 25 (6) (2016) 065009.
[26] S. Dey, T. Mukhopadhyay, H.H. Khodaparast, S. Adhikari, A response surface modelling approach for resonance driven reliability based optimization of composite shells, Periodica Polytech. Civ. Eng. 60 (1) (2016) 103–111.
[27] T. Mukhopadhyay, S. Adhikari, Stochastic mechanics of metamaterials, Compos. Struct. 162 (2017) 85–97.
[28] M.C. Smith, The inerter: a retrospective, Annu. Rev. Control, Robot., Auton. Syst. 3 (2020) 361–391.
[29] M.C. Smith, Synthesis of mechanical networks: the inerter, IEEE Trans. Autom. Control 47 (10) (2002) 1648–1662.
[30] L. Marian, A. Giaralis, Optimal design of a novel tuned mass-damper–inerter (TMDI) passive vibration control configuration for stochastically support-excited structural systems, Probab. Eng. Mech. 38 (2014) 156–164.
[31] D. Pietrosanti, M. De Angelis, M. Basili, Optimal design and performance evaluation of systems with tuned mass damper inerter (TMDI), Earthq. Eng. Struct. Dyn. 46 (8) (2017) 1367–1388.
[32] A. Giaralis, A. Taflanidis, Optimal tuned mass-damper-inerter (TMDI) design for seismically excited MDOF structures with model uncertainties based on reliability criteria, Struct. Control Health Monit. 25 (2) (2018) e2082.
[33] R. Ruiz, A. Taflanidis, A. Giaralis, D. Lopez-Garcia, Risk-informed optimization of the tuned mass-damper-inerter (TMDI) for the seismic protection of multi-storey building structures, Eng. Struct. 177 (2018) 836–850.
[34] Z. Zhao, Q. Chen, R. Zhang, C. Pan, Y. Jiang, Optimal design of an inerter isolation system considering the soil condition, Eng. Struct. 196 (2019) 109324.
[35] D. De Domenico, P. Deastra, G. Ricciardi, N.D. Sims, D.J. Wagg, Novel fluid inerter based tuned mass dampers for optimised structural control of base-isolated buildings, J. Frankl. Inst. 356 (14) (2019) 7626–7649.
[36] G. Moghimi, N. Makris, Seismic response of yielding structures equipped with inerters, Soil Dyn. Earthq. Eng. 141 (2020) 106474.
[37] D. Čakmak, Z. Tomičević, H. Wolf, Ž. Božić, D. Semenski, I. Trapić, Vibration fatigue study of the helical spring in the base-excited inerter-based isolation system, Eng. Fail. Anal. 103 (2019) 44–56.
[38] G. Barone, F.L. Iacono, G. Navarra, A. Palmeri, Closed-form stochastic response of linear building structures to spectrum-consistent seismic excitations, Soil Dyn. Earthq. Eng. 125 (2019) 105724.
[39] F. Petrini, A. Giaralis, Z. Wang, Optimal tuned mass-damper-inerter (TMDI) design in wind-excited tall buildings for occupants' comfort serviceability performance and energy harvesting, Eng. Struct. 204 (2020) 109904.
[40] D. Pietrosanti, M. De Angelis, M. Basili, A generalized 2-DOF model for optimal design of MDOFstructures controlled by tuned mass damper inerter (TMDI), Int. J. Mech. Sci. 185 (2020) 105849.
[41] Z. Zhu, W. Lei, Q. Wang, N. Tiwari, B. Hazra, Study on wind-induced vibration control of linked high-rise buildings by using TMDI, J. Wind Eng. Ind. Aerodyn. 205 (2020) 104306.
[42] A. Giaralis, L. Marian, Use of inerter devices for weight reduction of tuned mass-dampers for seismic protection of multi-story building: the tuned mass-damper-interter (TMDI), in: Active and Passive Smart Structures and Integrated Systems 2016, vol. 9799, International Society for Optics and Photonics, 2016, p. 97991G.
[43] Z. Zhang, B. Fitzgerald, Tuned mass-damper-inerter (TMDI) for suppressing edgewise vibrations of wind turbine blades, Eng. Struct. 221 (2020) 110928.
[44] L.A. Lara-Valencia, Y. Farbiarz-Farbiarz, Y. Valencia-González, Design of a tuned mass damper inerter (TMDI) based on an exhaustive search optimization for structural control of buildings under seismic excitations, Shock Vib. (2020).
[45] I. Lazar, S. Neild, D. Wagg, Vibration suppression of cables using tuned inerter dampers, Eng. Struct. 122 (2016) 62–71.
[46] I.F. Lazar, S.A. Neild, D.J. Wagg, Design and performance analysis of inerter-based vibration control systems, in: Dynamics of Civil Structures, vol. 4, Springer, 2014, pp. 493–500.
[47] D.J. Wagg, A review of the mechanical inerter: historical context, physical realisations and nonlinear applications, Nonlinear Dyn. 104 (1) (2021) 13–44.
[48] F. Qian, Y. Luo Sr, H. Sun, W.C. Tai, L. Zuo, Performance enhancement of a base-isolation structure using optimal tuned inerter dampers, in: Active and Passive Smart Structures and Integrated Systems XIII, vol. 10967, International Society for Optics and Photonics, 2019, p. 1096715.
[49] G. Muscolino, A. Palmeri, C. Versaci, Damping-adjusted combination rule for the response spectrum analysis of base-isolated buildings, Earthq. Eng. Struct. Dyn. 42 (2) (2013) 163–182.
[50] R. Zhang, Z. Zhao, K. Dai, Seismic response mitigation of a wind turbine tower using a tuned parallel inerter mass system, Eng. Struct. 180 (2019) 29–39.

[51] G. Bertollucci Colherinhas, F. Petrini, M.V.G. de Morais, F. Bontempi, Optimal design of passive-adaptive pendulum tuned mass damper for the global vibration control of offshore wind turbines, Wind Energy 24 (6) (2021) 573–595.
[52] L. Marian, A. Giaralis, Optimal design of inerter devices combined with TMDs for vibration control of buildings exposed to stochastic seismic excitation, in: Safety, Reliability, Risk and Life-Cycle Performance of Structures and Infrastructures-Proceedings of the 11th International Conference on Structural Safety and Reliability, ICOSSAR 2013, CRC Press, 2013, pp. 1025–1032.
[53] A. Giaralis, F. Petrini, Wind-induced vibration mitigation in tall buildings using the tuned mass-damper-inerter, J. Struct. Eng. 143 (9) (2017) 04017127.
[54] S. Chowdhury, A. Banerjee, S. Adhikari, Optimal design of inertial amplifier base isolators for dynamic response control of multi-storey buildings, Int. J. Struct. Stab. Dyn.(0) (ja) (0)10.1142/S0219455423500475
[55] C. Yilmaz, G. Hulbert, Theory of phononic gaps induced by inertial amplification in finite structures, Phys. Lett. A 374 (34) (2010) 3576–3584.
[56] C. Yilmaz, G.M. Hulbert, Dynamics of locally resonant and inertially amplified lattice materials, in: A.S. Phani, M.I. Hussein (Eds.), Dynamics of Lattice Materials, 2017, p. 233.
[57] C. Yilmaz, G.M. Hulbert, N. Kikuchi, Phononic band gaps induced by inertial amplification in periodic media, Phys. Rev. B 76 (5) (2007) 054309.
[58] S. Muhammad, S. Wang, F. Li, C. Zhang, Bandgap enhancement of periodic nonuniform metamaterial beams with inertial amplification mechanisms, J. Vib. Control 26 (15-16) (2020) 1309–1318. 1077546319895630
[59] J. Zhou, L. Dou, K. Wang, D. Xu, H. Ouyang, A nonlinear resonator with inertial amplification for very low-frequency flexural wave attenuations in beams, Nonlinear Dyn. 96 (1) (2019) 647–665.
[60] S. Taniker, C. Yilmaz, Design, analysis and experimental investigation of three-dimensional structures with inertial amplification induced vibration stop bands, Int. J. Solids Struct. 72 (2015) 88–97.
[61] A. Carrella, M. Brennan, T. Waters, Static analysis of a passive vibration isolator with quasi-zero-stiffness characteristic, J. Sound Vib. 301 (3–5) (2007) 678–689.
[62] A. Carrella, M. Brennan, I. Kovacic, T. Waters, On the force transmissibility of a vibration isolator with quasi-zero-stiffness, J. Sound Vib. 322 (4–5) (2009) 707–717.
[63] Z. Hao, Q. Cao, The isolation characteristics of an archetypal dynamical model with stable-quasi-zero-stiffness, J. Sound Vib. 340 (2015) 61–79.
[64] W.S. Robertson, M. Kidner, B.S. Cazzolato, A.C. Zander, Theoretical design parameters for a quasi-zero stiffness magnetic spring for vibration isolation, J. Sound Vib. 326 (1–2) (2009) 88–103.
[65] C. Cheng, S. Li, Y. Wang, X. Jiang, On the analysis of a high-static-low-dynamic stiffness vibration isolator with time-delayed cubic displacement feedback, J. Sound Vib. 378 (2016) 76–91.
[66] X. Huang, X. Liu, J. Sun, Z. Zhang, H. Hua, Vibration isolation characteristics of a nonlinear isolator using Euler buckled beam as negative stiffness corrector: a theoretical and experimental study, J. Sound Vib. 333 (4) (2014) 1132–1148.
[67] B.A. Fulcher, D.W. Shahan, M.R. Haberman, C. Conner Seepersad, P.S. Wilson, Analytical and experimental investigation of buckled beams as negative stiffness elements for passive vibration and shock isolation systems, J. Vib. Acoust. 136 (3) (2014).
[68] X. Liu, X. Huang, H. Hua, On the characteristics of a quasi-zero stiffness isolator using Euler buckled beam as negative stiffness corrector, J. Sound Vib. 332 (14) (2013) 3359–3376.
[69] A. Bhatt, A. Banerjee, Double attenuation peaks in metamaterial with simultaneous negative mass and stiffness, Phys. Lett. A 443 (2022) 128201. Elsevier, London, England
[70] Y. Zheng, X. Zhang, Y. Luo, B. Yan, C. Ma, Design and experiment of a high-static–low-dynamic stiffness isolator using a negative stiffness magnetic spring, J. Sound Vib. 360 (2016) 31–52.
[71] H. Iemura, M.H. Pradono, Advances in the development of pseudo-negative-stiffness dampers for seismic response control, Struct. Control Health Monit. 16 (7–8) (2009) 784–799.
[72] H. Iemura, A. Igarashi, M.H. Pradono, A. Kalantari, Negative stiffness friction damping for seismically isolated structures, Struct. Control Health Monit. 13 (2–3) (2006) 775–791.
[73] R.S. Lakes, T. Lee, A. Bersie, Y.-C. Wang, Extreme damping in composite materials with negative-stiffness inclusions, Nature 410 (6828) (2001) 565–567.
[74] X. Shi, S. Zhu, Simulation and optimization of magnetic negative stiffness dampers, Sens. Actuators, A 259 (2017) 14–33.
[75] W. Wu, X. Chen, Y. Shan, Analysis and experiment of a vibration isolator using a novel magnetic spring with negative stiffness, J. Sound Vib. 333 (13) (2014) 2958–2970.
[76] A. Banerjee, R. Das, E.P. Calius, Waves in structured mediums or metamaterials: a review, Arch. Comput. Methods Eng. 26 (4) (2019) 1029–1058.
[77] N.M. Frandsen, O.R. Bilal, J.S. Jensen, M.I. Hussein, Inertial amplification of continuous structures: large band gaps from small masses, J. Appl. Phys. 119 (12) (2016) 124902.
[78] H. Huang, C. Sun, Theoretical investigation of the behavior of an acoustic metamaterial with extreme Young's modulus, J. Mech. Phys. Solids 59 (10) (2011) 2070–2081.
[79] G.P. Cimellaro, M. Domaneschi, G. Warn, Three-dimensional base isolation using vertical negative stiffness devices, J. Earthq. Eng. 24 (12) (2020) 2004–2032.
[80] H. Li, Y. Li, J. Li, Negative stiffness devices for vibration isolation applications: a review, Adv. Struct. Eng. 23 (8) (2020) 1739–1755.
[81] T.D. Le, K.K. Ahn, A vibration isolation system in low frequency excitation region using negative stiffness structure for vehicle seat, J. Sound Vib. 330 (26) (2011) 6311–6335.
[82] S. Xiang, Z. Songye, A comparative study of vibration isolation performance using negative stiffness and inerter dampers, J. Frankl. Inst. 356 (14) (2019) 7922–7946.
[83] A. Dwivedi, A. Banerjee, B. Bhattacharya, Simultaneous energy harvesting and vibration attenuation in piezo-embedded negative stiffness metamaterial, J. Intell. Mater. Syst. Struct. 31 (8) (2020) 1076–1090.
[84] S. Chowdhury, A. Banerjee, S. Adhikari, Enhanced seismic base isolation using inertial amplifiers, Structures 33 (2021) 1340–1353, doi:10.1016/j.istruc.2021.04.089. https://www.sciencedirect.com/science/article/pii/S2352012421003908
[85] M. Barys, R. Zalewski, Analysis of inertial amplification mechanism with smart spring-damper for attenuation of beam vibrations, in: MATEC Web of Conferences, vol. 157, EDP Sciences, 2018, p. 03002.
[86] M. Barys, J.S. Jensen, N.M. Frandsen, Efficient attenuation of beam vibrations by inertial amplification, Eur. J. Mech. - A/Solids 71 (2018) 245–257.
[87] A. Bhatt, A. Banerjee, Flexural wave propagation in rigid elastic combined metabeam, J. Vib. Acoust. 145 (1) (2022) 011006.
[88] O. Yuksel, C. Yilmaz, Shape optimization of phononic band gap structures incorporating inertial amplification mechanisms, J. Sound Vib. 355 (2015) 232–245.
[89] Z. Cheng, A. Palermo, Z. Shi, A. Marzani, Enhanced tuned mass damper using an inertial amplification mechanism, J. Sound Vib. 475 (2020) 115267.
[90] O. Yuksel, C. Yilmaz, Realization of an ultrawide stop band in a 2-Delastic metamaterial with topologically optimized inertial amplification mechanisms, Int. J. Solids Struct. 203 (2020) 138–150.
[91] Y. Mi, X. Yu, Sound transmission of acoustic metamaterial beams with periodic inertial amplification mechanisms, J. Sound Vib. 499 (2021) 116009.
[92] A. Banerjee, S. Adhikari, M.I. Hussein, Inertial amplification band-gap generation by coupling a levered mass with a locally resonant mass, Int. J. Mech. Sci. 207 (2021) 106630.
[93] S. Adhikari, A. Banerjee, Enhanced low-frequency vibration energy harvesting with inertial amplifiers, J. Intell. Mater. Syst. Struct. 33 (6) (2021) 822–838. 1045389X211032281
[94] S. Chowdhury, A. Banerjee, The exact closed-form expressions for optimal design parameters of resonating base isolators, Int. J. Mech. Sci. 224 (2022) 107284.
[95] J.B. Roberts, P.D. Spanos, Random Vibration and Statistical Linearization, Courier Corporation, 2003.

[96] Y. Hu, M.Z. Chen, Z. Shu, L. Huang, Analysis and optimisation for inerter-based isolators via fixed-point theory and algebraic solution, J. Sound Vib. 346 (2015) 17–36.
[97] Y. Iwata, On the construction of the dynamic vibration absorbers, Japanese Soc. Mech. Eng. 820 (8) (1982) 150–152.
[98] G.B. Warburton, Optimum absorber parameters for various combinations of response and excitation parameters, Earthq. Eng. Struct. Dyn. 10 (3) (1982) 381–401.
[99] M. Zilletti, S.J. Elliott, E. Rustighi, Optimisation of dynamic vibration absorbers to minimise kinetic energy and maximise internal power dissipation, J. Sound Vib. 331 (18) (2012) 4093–4100.
[100] O. Nishihara, T. Asami, Closed-form solutions to the exact optimizations of dynamic vibration absorbers (minimizations of the maximum amplitude magnification factors), J. Vib. Acoust. 124 (4) (2002) 576–582.
[101] S. Krenk, Frequency analysis of the tuned mass damper(2005).
[102] A.K. Chopra, Dynamics of Structures, Pearson Education India, 2007.